UNIVERSITÀ DEGLI STUDI DI SALERNO

UNIVERSITÀ DEGLI STUDI DI SALERNO
Dipartimento di Farmacia

PhD Program
in **Drug Discovery and Development**
XXXVIII Cycle - Academic year 2024/2025

PhD Thesis in

Research and development through automated laboratory procedures

Candidate

Davide Romanini

Tutor

Prof. *Simona Concilio*

Co-tutor

Prof. *Stefano Piotto*

PhD Program Coordinator: Prof. *Alessandra Tosco*

Abstract

Model membrane systems, such as lipid monolayers and Giant Unilamellar Vesicles (GUVs), are indispensable tools in pharmaceutical sciences for investigating drug-membrane interactions. However, the adoption of the technologies needed for these studies is often hindered by the prohibitive cost of commercial instrumentation, the lack of customization, and data fragmentation across proprietary formats. This doctoral thesis addresses these technological barriers by developing an integrated, open-source ecosystem of hardware and software tools designed to democratize and automate membrane biophysics research.

First, a modular Langmuir-Blodgett trough was engineered using the Arduino platform. The system, controlled via a custom Python interface (LanGUImuir) and an automated protocol generator (ScriptMaker), provides precise control over barrier compression and surface pressure acquisition. Validation tests with anionic surfactants demonstrated a high signal-to-noise ratio (42.1 dB), and the device successfully resolved the thermodynamic phase transitions of complex biological monolayers (egg yolk phospholipids) with high linearity.

Second, the production of GUVs was optimized through the design of novel stainless steel mesh electrodes. A systematic evaluation of chamber geometries identified a specific configuration (Chamber D, Mesh 30) capable of achieving a lipid incorporation yield of 0.20% of unilamellar vesicles, significantly outperforming traditional indium tin oxide (ITO) methods in terms of cost, durability, and efficiency. The platform proved robust for handling complex ternary mixtures (POPC:SM:Chol) and was successfully applied to investigate membrane rigidity via Generalized Polarization (GP) and to validate the passive translocation of Cell-Penetrating Peptides (CPPs).

Finally, to bridge the gap between raw data and biological insight, a comprehensive computational framework was developed. This suite includes utilities for cross-platform spectral data standardization (DX2CSV) and an advanced deconvolution tool (Extrapolator). The latter significantly enhances the sensitivity of membrane fluidity measurements by resolving overlapping spectral components, offering a more robust metric than traditional intensity-based methods.

Collectively, this work demonstrates that high-quality biophysical data can be obtained using accessible, custom-built instrumentation. The developed platforms offer a scalable and flexible workflow for high-throughput membrane research, paving the way for more efficient drug screening and formulation development.

Graphical Abstract

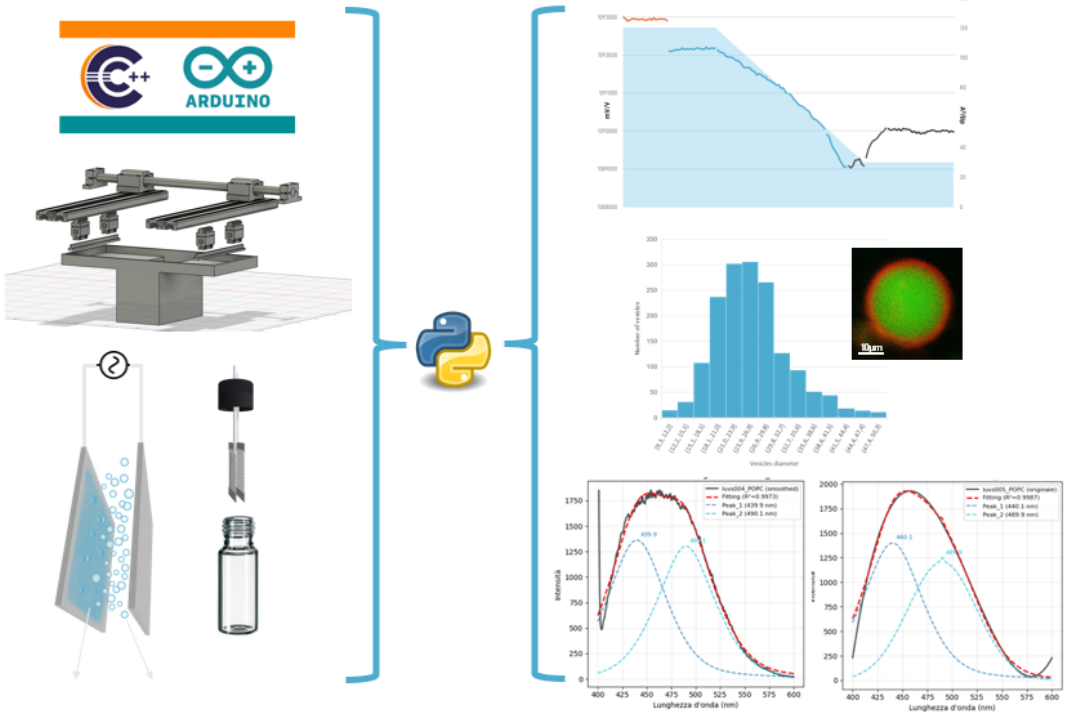

List of publications and conference proceedings related to the scientific activity performed during the three-year Ph.D. course in Drug Discovery and Development

Papers:

L. Sessa, S. Concilio, M. Di Martino, **D. Romanini**, X. Busquets, S. Piotto, Bending the rules: molecular dynamics of hydroxylated sphingolipid membranes with 2-hydroxyoleic acid, *Chemistry and Physics of Lipids* 2025, 268, 105475 – *DOI: https://doi.org/10.1016/j.chemphyslip.2025.105475.*

P. Albanese, C. Amante, S. Cataldini, M. Colombo, M. Di Martino, K. Jacob, Y. Jocmara, I. Maromatidou, **D. Romanini**, C. Pierro, N. Valletti, C. Sardo, L. Sessa, J. Chen, S. Concilio, P. Del Gaudio, G. Pilet, S. Piotto, F. Rossi, M. Fiore, 1-(4-Aminophenoxy)-3-(alkyl)propane-2-ols as Building Blocks for the Preparation of Membranogenic Compounds, *ChemistrySelect* 2025, 10 (30), e03367 – *DOI: https://doi.org/10.1002/slct.202503367.*

D. Romanini; M. Martino; L. Sessa; S. Concilio; S. Piotto, Electroformation of Giant Unilamellar Vesicles: Novel Electrode Design and Parameters for Enhanced GUVs Production, *Bioelectrochemistry* 2026, 169, 109192 – *DOI: https://doi.org/10.1016/j.bioelechem.2025.109192.*

K. Jacob; C. Pierro; **D. Romanini**; S. Mebarek; M. Fiore, Liposome-Based Potential Vaccines Platforms that are non-Cytotoxic. *ChemistryOpen* 2026, 15, e202500530 - DOI: *https://doi.org/10.1002/open.202500530.*

Conference:

25ÈME JOURNÉE ANNUELLE IMBL – 8ÈME JOURNÉE ANNUELLE MATSAN - 10-11 June 2025 Villeurbanne (France)

D. Romanini, T. Granjon, O. Maniti, A. Girard-Egrot, A. Trunfio-Sfarghiu, S. Piotto, S. Concilio, Versatile and Durable Electroformation Systems for Automated and Scalable Application.

Table of Contents

CHAPTER 1

General Introduction

1.1 Model membrane systems in pharmaceutical sciences

The evolution of membrane model systems has significantly advanced our understanding of pharmaceutical sciences, particularly in the realms of drug delivery and membrane interactions. Historically, the development of vesicular systems (Figure 1), such as small unilamellar vesicles (SUVs, 20-100nm), large unilamellar vesicles (LUVs, 100-1000nm), and giant unilamellar vesicles (GUVs, 1-200 μm) [1], has provided crucial insights into the behaviour of biological membranes.

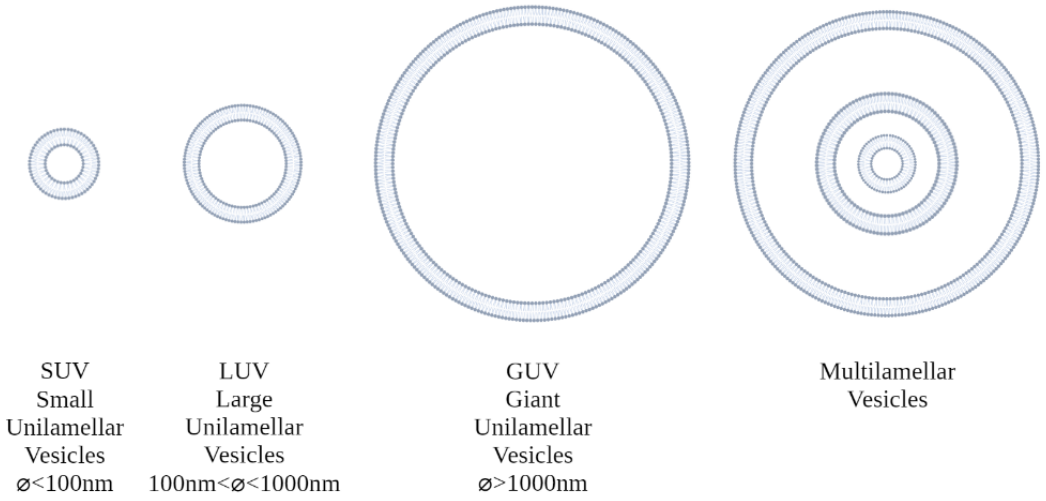

Figure 1 *Classification of SUVs, LUVs, GUV, MLV.*

These vesicular structures mimic cellular membranes, enabling researchers to explore the complexities of drug-membrane interactions in controlled environments. Vesicles such as liposomes, as well as Langmuir monolayers, are among the most widely used model membrane systems, offering well-defined architectures for investigating drug effects on membrane structure and permeability [2, 3]. Coupled with lipid monolayers, which provide a simplified representation of membrane dynamics, these systems form a pivotal platform in drug formulation processes, facilitating the investigation of how pharmaceutical

compounds navigate biological barriers. The use of biomimetic lipid systems, including monolayers and vesicular membranes, allows rigorous control of physicochemical parameters under conditions not feasible in live cells [4, 5].

Current methodologies regarding vesicle preparation, including extrusion and sonication, alongside advanced characterisation techniques, such as fluorescence microscopy, confocal microscopy and atomic force microscopy, offer a comprehensive framework for elucidating the mechanisms governing drug absorption and efficacy in the human body, providing nanoscale insights into vesicle morphology, mechanical properties, and surface ligand modifications under physiologically relevant conditions [6], or evaluating membrane mechanical parameters such as rigidity, useful in tailored drug delivery systems for specific affinity [7, 8]. Functionalisation strategies applied to lipid membranes, such as the incorporation of targeting ligands, responsive probes, or structural modifiers, enhance their specificity, stability, and adaptability [9, 10]. These modifications are particularly relevant in the design of vesicular systems and Langmuir-Blodgett monolayers, where controlled surface properties enable precise investigation of drug-membrane interactions and targeted delivery mechanisms [11, 12]. The exploration of lipid compositions and the influence of various lipid phases create diverse environments for drug testing [13, 14].

While Surface Plasmon Resonance (SPR) provides valuable real-time data on molecular interactions at membrane interfaces [15], complementary approaches such as the use of membrane-responsive probes in vesicle systems [16] or Langmuir-Blodgett techniques for monolayer and bilayer construction [11, 17, 18] enable more physiologically relevant or structurally controlled environments. These methods allow for the fine-tuning of lipid composition, surface pressure, and membrane fluidity, offering deeper insights into drug partitioning and membrane permeability.

In the past decade, high-resolution structures of many membrane transporters have been experimentally determined, further reinforcing the role of artificial membrane systems in drug research [19] and recent advances in computational modelling now allow for the simulation of membrane dynamics, offering deeper insights into drug transport mechanisms [20]. Techniques such as nanodiscs and liposome reconstitution have proven essential for stabilizing membrane proteins in near-native environments, enabling structural and functional studies [21, 22].

Ultimately, the ongoing refinement of vesicle technologies is pivotal for pioneering, applications in the pharmaceutical industry. Indeed, liposomal packaging of Wnt proteins has been shown to enhance and sustain their biological activity in vitro and in vivo, mimicking natural transport mechanisms of signaling molecules [23]. Recent investigations have highlighted the role of membrane components, such as lipid rafts and protein complexes, in modulating drug interactions, unveiling novel therapeutic targets. For example, insights from Wnt signalling pathways suggest a link between membrane dynamics and cancer stem cell maintenance, indicating that disrupting these interactions may offer new strategies in oncology[24]. The exploration of lipid compositions and the influence of various lipid phases create diverse environments for drug testing. Simultaneously, biomimetic membrane vesicles serve as drug delivery systems whose biodistribution and in vivo administration routes require rigorous optimization to ensure biocompatibility and regulatory compliance [25]. In parallel, the rise of multidrug-resistant organisms and the limitations of conventional antibiotics have made membrane model systems indispensable for simulating and evaluating novel antimicrobial agents under physiologically relevant conditions [26]. Furthermore, emerging therapeutic modalities, such as RNA interference therapies, have greatly benefited from these models, enabling the development of targeted delivery strategies with enhanced tissue specificity [27, 28].

Recent developments have highlighted the role of lipid monolayers as foundational tools for investigating membrane phenomena at the molecular level, offering valuable insights for the design of lipid-based drug delivery systems. As elaborated by Danaei et al.[29], lipid carriers not only protect drugs from premature degradation but also facilitate controlled release, making them imperative in modern therapeutic strategies. These experimental systems elucidate the complex interactions between drugs and lipid membranes, guiding the development of advanced formulations. Moreover, the ability to study how biostimulants, such as microbial agents, interact with membranes at a detailed level highlights the potential of these systems to inform regulatory frameworks and commercial applications.

Over the past two decades, membrane model systems have continued to evolve, reinforcing their central role in pharmaceutical research.

The integration of vesicle and lipid research into pharmaceutical sciences may offer promising solutions for drug development, particularly in improving permeability, targeting, and reducing reliance on animal testing [9, 30]. By simulating physiological conditions, membrane model systems could support the evaluation of novel compounds and guide formulation strategies. Their interdisciplinary nature, bridging biochemistry, pharmacology, and materials science, positions them as valuable tools for advancing translational research and accelerating therapeutic innovation [31, 32].

1.1 Comparative overview of membrane model systems

The diversity of membrane model systems offers researchers a versatile toolkit for investigating drug-membrane interactions, each with distinct advantages and limitations.

Vesicular systems, provide three-dimensional, enclosed environments that closely mimic biological membranes. Their ability to encapsulate therapeutic

agents makes them ideal for drug delivery studies [9, 29]. However, they often suffer from issues of aggregation, limited long-term stability, and challenges in scaling production while maintaining uniformity [8, 33].

Langmuir-Blodgett monolayers (Figure 2) allow for precise control over lipid composition and surface pressure, making them excellent for studying thermodynamic properties and molecular interactions at the air–water interface [2, 34]. Despite their high reproducibility, they lack the structural complexity of bilayers and are limited to two-dimensional analysis.

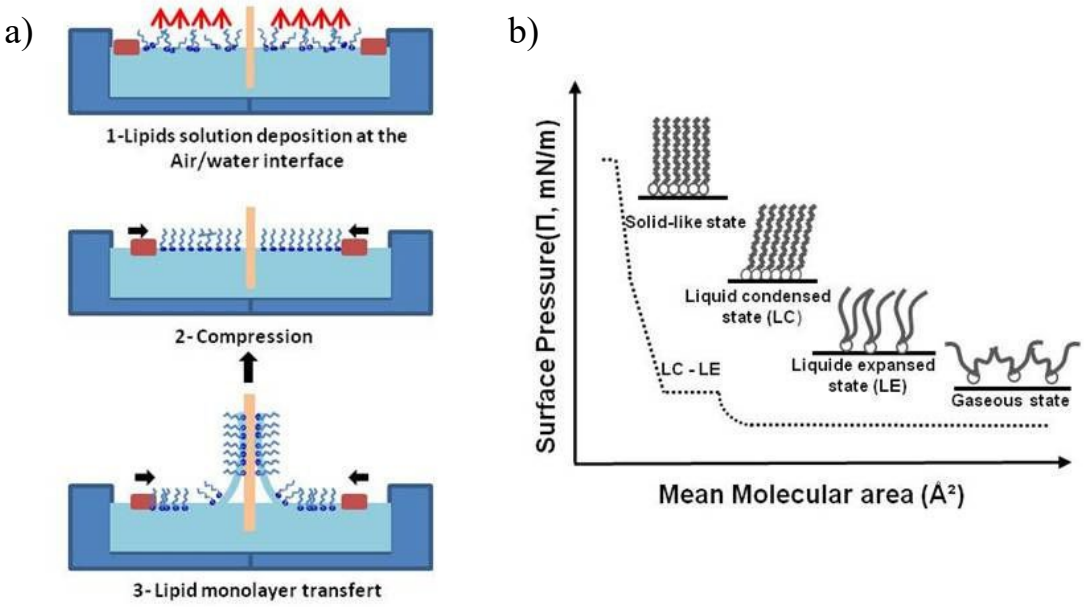

Figure 2 a) Langmuir-Blodgett principle, b) Theoretical isotherm (Π-A) obtained by compressing an insoluble lipid monolayer formed at an air / water (or buffer) interface [35]

Supported lipid bilayers, typically formed on solid substrates like glass or mica, offer a stable and planar platform for investigating membrane-associated processes, including protein-lipid interactions. Their compatibility with surface-sensitive techniques (e.g., AFM, SPR) is a major strength [36, 37], though the presence of the support can interfere with membrane fluidity and protein mobility [38].

Nanodiscs, composed of lipid bilayers stabilized by scaffold proteins or polymers, provide a native-like lipid environment in solution, particularly suited for structural and functional studies of membrane proteins [21, 39]. They offer high homogeneity and compatibility with spectroscopic techniques, but are not designed for drug delivery and require complex assembly protocols.

Altogether, the choice of membrane model depends on the experimental objective, whether it be mechanistic insight, structural analysis, or therapeutic application, and must balance physiological relevance with technical feasibility.

1.2 Vesicle preparation

In biotechnology, vesicle preparation has been proven useful for the encapsulation and delivery of therapeutic agents and bioactive molecules and for the study of membranes [40-42]. This section outlines the principal methodologies, freeze–thaw cycling, extrusion, and electroformation, each offering distinct advantages and limitations tailored to specific biomedical applications. Freeze–thaw is valued for its simplicity and cost-effectiveness, extrusion enables fine control over vesicle size and homogeneity, while electroformation provides customizable platforms for high-capacity vesicle production, and the microfluidic approaches are the most scalable. These techniques critically influence vesicle functionality and therapeutic efficacy, with future innovations poised to enhance their clinical relevance.

Vesicles, lipid bilayer-enclosed structures, are essential carriers in drug delivery and gene therapy. Lipid-based vesicles such as liposomes and niosomes enhance therapeutic selectivity and reduce systemic toxicity. Their chemical versatility allows for ligand functionalization, enabling targeted delivery to diseased cells. Preparation methods like freeze–thaw, extrusion, and electroformation facilitate precise control over vesicle size and physicochemical properties, which are crucial for optimizing therapeutic performance [43].

1.2.1 Freeze thaw

The freeze–thaw method (Figure 3) is a foundational approach for vesicle fabrication, particularly effective in enhancing drug encapsulation and stabilizing delivery systems. Rapid freezing preserves structural integrity, followed by controlled thawing that reorganizes lipid bilayers. This cyclic thermal modulation improves drug loading efficiency and release kinetics [44].

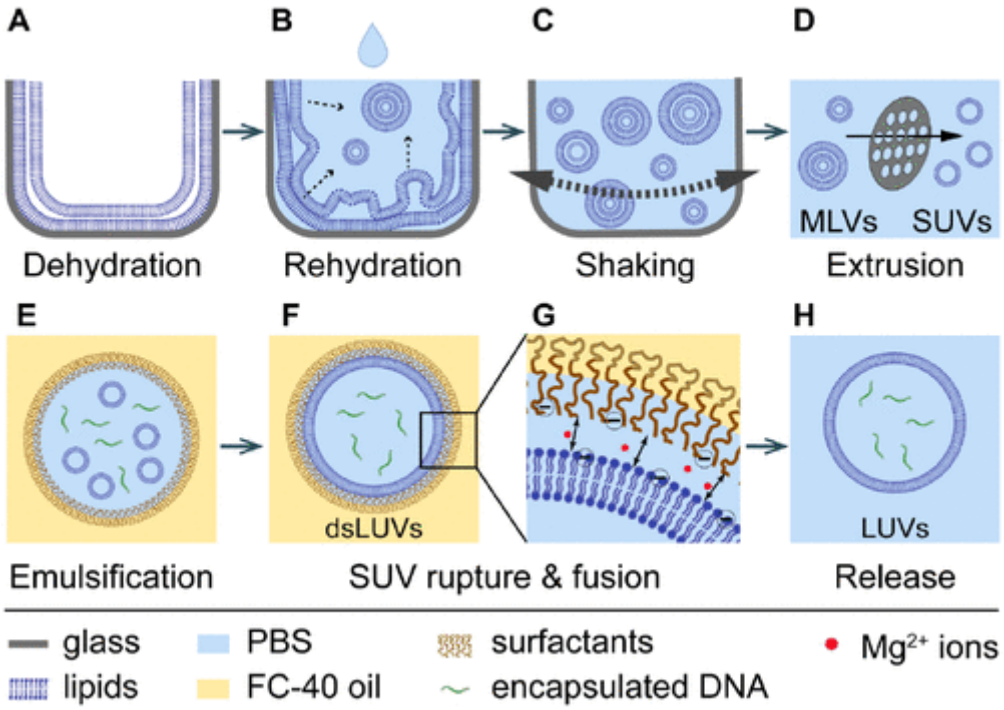

Figure 3 *Schematic overview of LUV formation via Freeze–Thaw and extrusion. Multilamellar vesicles (MLVs) are produced by drying (A) and rehydrating (B) a lipid film, then shaking (C). The MLVs are converted into SUVs by extrusion (D). Emulsification generates surfactant-stabilized water-in-oil droplets containing SUVs (E), where charge-mediated rupture and fusion at the droplet interface lead to the formation of a larger vesicle (F, G). Finally, the vesicles are released into aqueous buffer through surfactant destabilization (H) [45].*

However, optimization of freezing parameters is critical to prevent ice crystal formation, which may compromise vesicle stability [46]. Freeze–thaw cycles induce lipid concentration via ice crystallization, promoting self-assembly and encapsulation efficiency. Controlled thawing maintains vesicle integrity and minimizes leakage. Advanced techniques such as surface-initiated polymerization and self-assembly have enabled the generation of non-liposomal

lipid nanovesicles with tailored morphologies [47]. These innovations enhance nanomedicine applications by improving drug stability and delivery precision [48, 49].

1.2.2 Extrusion technique

Extrusion is a widely adopted method for the preparation of lipid vesicles, particularly liposomes, due to its ability to produce populations with controlled size and high uniformity. The process involves forcing multilamellar vesicles (MLVs), obtained usually with freeze thawing, through polycarbonate membranes with defined pore diameters under controlled pressure and temperature conditions (Figure 3). This mechanical shearing reorganizes the lipid bilayers, resulting in the formation of unilamellar vesicles with reduced size and polydispersity.

The extrusion process is typically repeated multiple times to ensure homogeneity, and the final vesicle size is largely determined by the pore size of the membrane used. For example, extrusion through 100 nm pores yields vesicles with diameters closely matching the membrane specification, often with a polydispersity index (PDI) below 0.2, indicating a narrow size distribution [50].

This technique significantly impacts vesicle performance:

- Size reduction enhances cellular uptake and tissue penetration, which are critical for drug delivery applications [51].
- Uniformity improves pharmacokinetic profiles and reduces variability in therapeutic response [51].
- Reproducibility makes extrusion suitable for both research-scale and industrial-scale production of liposomal formulations [52].

Moreover, extrusion facilitates the encapsulation of hydrophilic and hydrophobic compounds by stabilizing the lipid bilayer structure during vesicle

formation. The method is compatible with various lipid compositions and can be integrated with downstream processes such as surface functionalization or lyophilization.

1.2.3 Electroformation technique

Electroformation is an advanced method for generating vesicles that relies on the application of alternating electric fields to promote the self-assembly of lipid bilayers into giant unilamellar vesicles (GUVs). This approach offers precise control over vesicle morphology, size, and membrane composition, making it particularly suitable for applications in drug delivery, synthetic biology, and membrane biophysics.

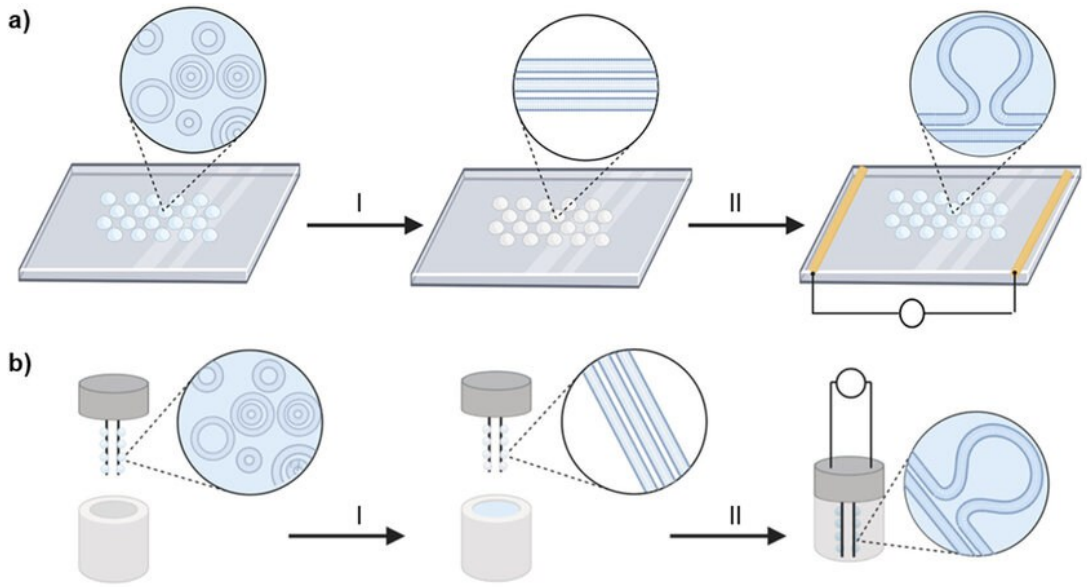

Figure 4 *Electroformation of giant vesicles and their morphology. Schematic representation of the GUV electroformation setups using ITO-coated glass slides (a) or platinum wires (b). Large liposomes applied on the indicated surfaces are partially dehydrated (step I). Subsequently, liposomes are rehydrated in GUV formation buffer in the presence of an AC electric field (step II), resulting in the formation of giant vesicles [53].*

The process (Figure 4) typically begins with the deposition of a thin lipid film onto conductive substrates, such as indium tin oxide (ITO)-coated glass slides, or platinum wires. Upon hydration in an aqueous medium and exposure to an electric field, the lipids undergo swelling and detachment from the substrate,

leading to the formation of vesicles with diameters ranging from several to tens of micrometers [43]. The resulting vesicles exhibit high reproducibility and structural integrity, which are essential for encapsulating macromolecules and studying membrane dynamics.

Electroformation has proven particularly valuable in the development of compartmentalized drug delivery systems and artificial cells. The large internal volume and customizable membrane composition of electroformed vesicles allow for the encapsulation of complex payloads, including enzymes, nucleic acids, and nanoparticles [54]. Furthermore, the technique supports the incorporation of ion channels and membrane proteins, enabling functional studies of transport mechanisms and signal transduction [55, 56].

Recent investigations have highlighted the role of electroformation in vesicle fusion, emphasizing the influence of lipid composition and ionic conditions on fusion efficiency. For example, cation-mediated fusion has been shown to depend on the presence of specific lipid species and membrane tension, which are critical parameters in designing responsive vesicle systems capable of targeted release or inter-vesicle communication [57].

1.2.4 Microfluidic technique

Microfluidic technology represents a transformative approach in vesicle fabrication, offering precise control over size, composition, and encapsulation efficiency. Unlike conventional bulk methods, which often rely on stochastic self-assembly, microfluidic systems (Figure 5) exploit laminar flow and confined geometries to direct the formation of vesicles with high monodispersity and reproducibility. This precision is particularly advantageous in biomedical applications where vesicle uniformity directly influences pharmacokinetics, biodistribution, and therapeutic efficacy.

The process typically involves the generation of single or double emulsions within microchannels, where amphiphilic molecules self-assemble into

vesicular structures under tightly regulated flow conditions. By adjusting flow rates, channel dimensions, and surfactant concentrations, researchers can finely tune vesicle size, selecting the filter used, achieving diameters between 70 and 170 nanometers with polydispersity indices as low as 0.16 [58]. Such control enables the production of vesicles that exhibit rapid cellular internalization and sustained biocompatibility, with uptake efficiencies exceeding 95% within a few hours and cell viability remaining above 85% over extended periods.

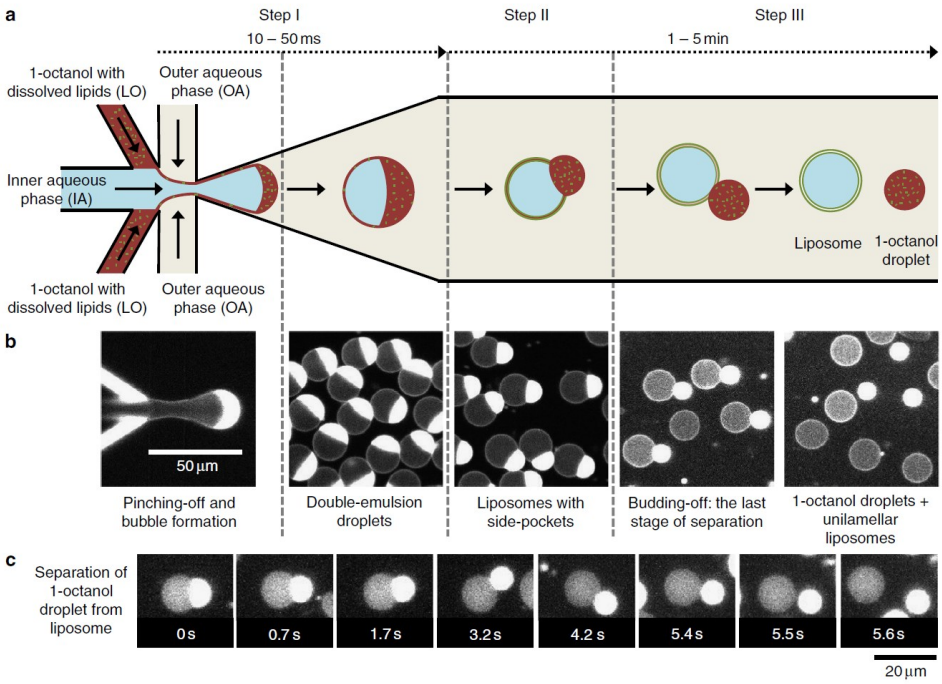

Figure 5 *Schematic representation showing the working principle of on-chip production of liposomes using microfluidic, on-chip liposome production using the Octanol-assisted Liposome Assembly method [59].*

Microfluidic emerged as the gold standard for the production of **Lipid Nanoparticles (LNPs)**, distinguishing them from traditional hollow vesicles. Unlike liposomes, which possess an aqueous core surrounded by a lipid bilayer, LNPs exhibit a solid or electron-dense core structure, often formed by the electrostatic complexation of ionizable lipids with nucleic acids (e.g., mRNA, siRNA). The rapid mixing regime achievable in microfluidic channels (<10 ms) allows for the controlled precipitation of these lipid components from an ethanolic phase into an aqueous buffer. This "bottom-up" assembly ensures

uniform particle size and high encapsulation efficiency, overcoming the structural limitations of conventional bulk preparation methods and representing the current frontier in lipid-based drug delivery [60, 61].

Despite these advantages, microfluidic systems present several limitations that hinder their broader clinical translation. One of the most critical challenges is the difficulty in controlling membrane composition, particularly the incorporation of cholesterol. Cholesterol plays a fundamental role in modulating membrane fluidity, permeability, and mechanical stability, yet its distribution within microfluidically generated vesicles often lacks uniformity due to rapid mixing dynamics and limited residence time during assembly [62]. This can lead to inconsistencies in vesicle behavior, affecting drug release profiles and membrane integrity under physiological conditions.

Additional concerns include residual solvent contamination, batch-to-batch variability, and the complexity of scaling up production while maintaining vesicle quality. The architecture of microfluidic channels and the physicochemical properties of the lipid formulation significantly influence vesicle characteristics, making standardization across platforms challenging [63]. These factors underscore the need for further optimization of microfluidic protocols and device design to ensure reproducibility and functional reliability in therapeutic applications.

1.2.5 Characterization methods

The accurate characterization of membrane model systems, ranging from simple monolayers to complex vesicular architectures, demands a multi-faceted analytical approach capable of transcending simple visualization. Since no single technique can provide a complete phenotyping, the integration of complementary methodologies is essential to achieve a holistic understanding of both structural topology and thermodynamic behavior [1].

To examine membrane topography and mechanical properties at the nanoscale, Atomic Force Microscopy (AFM) is widely regarded as the gold standard. Unlike electron microscopy, AFM operates effectively under physiological conditions without requiring sample fixation or dehydration, thereby enabling high-resolution imaging of hydrated vesicles in their native state [64]. This capability is critical for differentiating between unilamellar and multilamellar structures, as recent biomechanical studies have demonstrated a linear correlation between the degree of lamellarity and membrane stiffness, estimated at approximately 2.7×10^{-3} Nm^{-1} per bilayer [65].

Furthermore, AFM provides precise topographical data, such as the height of flattened vesicles (typically 1.8–2.5 nm), allowing for the sensitive detection of drug-induced morphological modifications [66, 67]. While AFM excels in single-particle mechanics, Dynamic Light Scattering (DLS) remains the preferred method for obtaining bulk statistical data on vesicle size distribution and suspension stability [29]. However, DLS is inherently limited by its assumption of spherical geometry and its high sensitivity to larger particles, which can skew results in polydisperse populations. Consequently, DLS data are most reliable when validated by imaging techniques like AFM, which can resolve bimodal distributions or aggregates often misinterpreted by light scattering algorithms [68].

Moving beyond static structure, characterizing the dynamic behavior of the lipid bilayer is fundamental for predicting drug delivery performance. Fluorescence Microscopy serves as the primary tool for visualizing lipid distribution and membrane fluidity [69]. Advanced implementations, such as epifluorescence microscopy, allow for the observation of phospholipid monolayers at the air-water interface, revealing how lipid microdomains and phase coexistence emerge from the competition between line tension and electrostatic repulsion [70]. More recently, combined reflectance and fluorescence confocal microscopy has enhanced the capability to distinguish

extracellular vesicle subpopulations through multiparametric detection [71]. To quantify molecular mobility within these systems, Fluorescence Recovery After Photobleaching (FRAP) is utilized to evaluate diffusion dynamics and lipid phase transitions, providing insights into how pharmaceutical substances alter membrane properties [72]. Recent technological optimizations have minimized the delay between bleaching and acquisition, enabling the study of rapid cytoskeletal dynamics and molecular assemblies [73]. Complementing this, Fluorescence Correlation Spectroscopy (FCS) offers superior sensitivity at low fluorophore concentrations; by analyzing fluorescence fluctuations in a confocal volume, FCS can determine diffusion coefficients and aggregation states of molecules that might be too dilute for FRAP analysis [74, 75].

Finally, when the focus shifts to intermolecular interactions at the nanometer scale, Förster Resonance Energy Transfer (FRET) provides the necessary resolution to detect conformational changes and protein-lipid interactions that are invisible to standard microscopy [76, 77]. This technique is particularly powerful for mapping membrane microheterogeneities and domain-specific organizations. In parallel, Fluorescence Lifetime Imaging Microscopy (FLIM) adds a further dimension by monitoring the environmental sensitivity of fluorophores. By measuring lifetime changes rather than intensity, FLIM reveals variations in local polarity and microviscosity, enabling the robust detection of lipid phases and three-phase coexistence that would otherwise remain indistinguishable [78].

1.3 Monolayer Techniques

1.3.1 Langmuir Balance

The Langmuir monolayer technique enables lipid film formation on water subphases and characterization of lipid-lipid, lipid-water, or lipid-drug interactions based on compression isotherms. These isotherms, obtained by measuring surface pressure (π) of the interfacial monolayer as a function of

mean molecular area (A), provide fundamental information on system thermodynamic properties [11].

The Langmuir balance typically uses the Wilhelmy method for surface pressure measurement, where automated barriers ensure precise control of film compression rate. During monolayer compression, different states can be observed: liquid-expanded (LE) and liquid-condensed (LC), analogous to liquid-crystalline and gel states in bilayers, respectively [79, 80].

The surface compressional modulus (Cs^{-1}) provides information on monolayer stiffness and lateral packing elasticity. Higher maximum compressibility modulus values indicate greater rigidity (decreased compressibility) of the monolayer [81]. Recent advances have made novel in situ methods available to study liquid interfaces with microscopic and molecular resolution, enhancing monolayer characterization capabilities.

1.3.2 Langmuir-Blodgett (LB) Techniques

Langmuir-Blodgett techniques enable controlled monolayer deposition on solid substrates, allowing ex-situ characterization using various complementary techniques [82, 83]. The quality of transferred monolayers is greatly enhanced using ultraclean, hydrophilic substrates with low surface roughness, yielding more well-packed, uniform films [84].

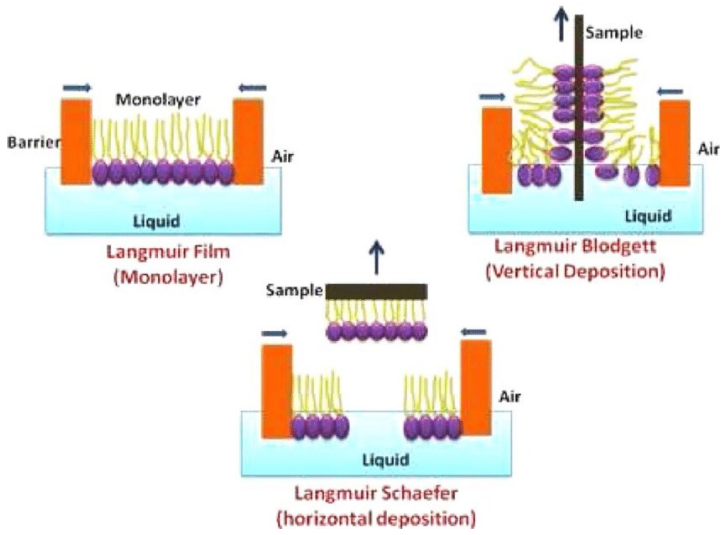

Figure 6 *Schematic diagram of Langmuir film, Langmuir Blodgett (vertical deposition) and Langmuir Schaefer (Horizontal deposition) techniques [85].*

LB deposition (Figure 6) can be performed in vertical mode (Langmuir-Blodgett proper) or horizontal mode (Langmuir-Schaefer). The transfer ratio (t.r.), defined as the ratio between monolayer area decrease during a deposition stroke and substrate area, is a critical parameter for evaluating deposition quality, with ideal transfer showing t.r. = 1. Modern LB troughs provide unique advantages in nanoparticle deposition, enabling precise control of molecular packing density and deposited layer thickness.

1.3.3 Complementary Techniques

Beyond the primary structural and morphological analyses, a complete physicochemical profiling of model membranes requires techniques capable of probing thermodynamic stability, interaction kinetics, and population heterogeneity.

To investigate the phase behavior and thermal stability of lipid bilayers, Differential Scanning Calorimetry (DSC) is the methodology of choice. By measuring the heat capacity of the system as a function of temperature, DSC allows for the precise determination of the gel-to-fluid phase transition temperature (T_m) and the cooperativity of the process. This technique is

particularly valuable for assessing how environmental factors or the insertion of pharmacological agents perturb bilayer integrity and packing order [86].

For real-time monitoring of binding events at the membrane interface, SPR provides kinetic data without the need for labeling. It is extensively used to quantify the affinity and association/dissociation rates of drugs or biomolecules interacting with supported lipid bilayers [87]. Complementing this, Quartz Crystal Microbalance with Dissipation (QCM-D) measures nanogram-level mass variations and viscoelastic properties. Unlike SPR, QCM-D is sensitive to the hydration water coupled to the adsorbed film, allowing for the detection of conformational changes and structural rearrangements in the membrane upon drug binding [88].

While DLS provides ensemble statistics, Nanoparticle Tracking Analysis (NTA) offers a higher resolution for sizing polydisperse populations by tracking the Brownian motion of individual particles. This particle-by-particle approach allows for the determination of size distribution profiles and precise concentration (particles/mL) measurements, which are often obscured in bulk scattering techniques. Furthermore, NTA can operate in fluorescence mode to specifically detect labeled subpopulations, distinguishing drug-loaded vesicles from empty aggregates [89].

1.3.4 Integrated Approaches and Future Perspectives

Integration of multiple characterization techniques is essential for a comprehensive understanding of membrane model systems. Currently, no single method allows phenotyping, sizing, and enumerating the whole range of extracellular vesicles; therefore, a combination of methods is needed, which might include electron and atomic force microscopy alongside full RNA, lipid, and protein profiling. The described techniques enable investigation of phenomena spanning nanosecond to second timescales and nanometric to micrometric spatial resolutions. This multidisciplinary approach is crucial for

developing more effective drug delivery systems and optimizing therapeutic strategies [90]. Recent advances in integrating complementary techniques, such as combining confocal reflectance and fluorescence microscopy to distinguish extracellular vesicle subpopulations, demonstrate the potential of multiparametric approaches for more complete and accurate characterizations[71]. The continued evolution of these characterization methods, supported by innovations in nanomaterial synthesis and application of Green Chemistry principles, continues to strengthen the central role of membrane model systems in pharmaceutical sciences, opening new possibilities for developing advanced therapies and next-generation drug delivery systems [91].

Applications in the Study of Drug-Membrane Interactions

The application of membrane model systems has fundamentally transformed the landscape of pharmaceutical research, particularly by enabling the transition from theoretical pharmacology to the clinical reality of nanomedicine. Since the first description of liposomal formulations nearly six decades ago, lipid vesicles have evolved into sophisticated carriers for drug and gene delivery. Today, several formulations have achieved clinical approval for cancer chemotherapy, including carriers for doxorubicin, irinotecan, and paclitaxel, demonstrating the translational power of these models [92]. Among the various architectures, Small Unilamellar Vesicles (SUVs) and Large Unilamellar Vesicles (LUVs) have emerged as the optimal platforms, balancing the capacity to encapsulate both hydrophilic and lipophilic payloads with the structural integrity required for systemic circulation [29].

Beyond simple encapsulation, lipid monolayers and bilayers serve as indispensable tools for elucidating the mechanisms of membrane permeability. The partitioning of small molecules into cell membranes—a critical predictor of bioavailability—is governed by thermodynamic principles that can be accurately modeled in these synthetic systems [93].

Advanced preparation techniques, such as electroformation and extrusion, allow researchers to tailor the lipid composition to replicate specific biological barriers. This control is vital, as the drug release rate is strictly dependent on the physicochemical properties of the phospholipid bilayer that the active compound must traverse [94]. Consequently, these models permit the systematic investigation of how membrane fluidity, phase behavior, and composition directly modulate transport kinetics.

The utility of membrane models extends to the optimization of targeted therapeutic strategies. In the realm of biologics, GUVs have proven instrumental in deciphering antibody-membrane interactions, revealing how lipid composition influences antibody conformation and binding affinity [95, 96]. This molecular-level insight facilitates the engineering of monoclonal antibodies with enhanced specificity and reduced immunogenicity. Simultaneously, these systems are essential for validating passive targeting mechanisms, such as the Enhanced Permeability and Retention (EPR) effect. Unlike healthy tissues with tight endothelial junctions, tumor tissues exhibit a leaky vasculature (pores of 100 nm–2 μm) that allows liposomes to extravasate and accumulate selectively at the disease site [97]. Once at the target, the interaction is governed by fusion and uptake mechanisms. Membrane models have helped elucidate the factors influencing liposome-cell interactions—such as surface charge, diameter, and ligand functionalization—distinguishing between specific receptor-mediated endocytosis, direct fusion, or non-specific adsorption [98].

Future Perspectives: From Stability to Smart Materials

Finally, the evolution of membrane technology is paving the way for "smart" drug delivery systems capable of responding to environmental stimuli. Innovations such as carbon nanotubes represent a new class of molecular transporters, showing potential for intracellular protein delivery both *in vitro* and *in vivo* [99]. Similarly, the modulation of vesicle physicochemical

properties has emerged as a powerful strategy to engineer "smart bullets" for precision medicine. Recent studies have demonstrated that **tuning membrane fluidity** allows for the selective targeting of cancer cells, enhancing therapeutic efficacy through specific fusion mechanisms [7]. The continuous refinement of these models, integrated with rigorous characterization techniques like AFM and DLS to ensure stability, remains paramount. This paradigm shift towards nanomedicine not only amplifies the efficacy of traditional therapies but provides essential tools to address complex pathologies and the growing challenge of multidrug resistance [100].

1.4 Limitations of Membrane Model Systems and Current Challenges

1.4.1 Vesicle Preparation Limitations

Freeze-Thaw Methodology Constraints

Despite its widespread use, the freeze-thaw method presents several critical limitations that can compromise vesicle integrity and reproducibility. Ice crystal formation during rapid freezing can induce mechanical stress on lipid bilayers, potentially leading to membrane disruption and heterogeneous vesicle populations [44]. The cyclic thermal modulation, while effective for drug encapsulation enhancement, may result in lipid oxidation and degradation, particularly for unsaturated phospholipids sensitive to temperature fluctuations [46]. Additionally, the method offers limited control over final vesicle size distribution, often yielding multilamellar vesicles with high polydispersity indices that require subsequent processing steps.

Extrusion Technique Limitations

While extrusion provides excellent size control and homogeneity, it suffers from several operational constraints. The mechanical shearing forces applied during membrane passage can damage sensitive encapsulated materials, including proteins and nucleic acids, reducing their biological activity [50]. The technique is particularly challenging for viscous formulations or those containing high cholesterol concentrations, which may require elevated temperatures that could compromise thermolabile compounds. Furthermore, membrane fouling and pore blocking during repeated extrusion cycles can lead to inconsistent results and require frequent membrane replacement, increasing operational costs and complexity [51].

Electroformation Technical Challenges

Electroformation, despite producing high-quality GUVs, presents significant scalability and reproducibility issues. The technique requires specialized equipment and expertise, making it less accessible for routine pharmaceutical applications. Vesicle formation is highly sensitive to ionic strength, pH, and lipid composition, with even minor variations leading to failed or inconsistent vesicle generation [43] . The presence of charged molecules or salts in the medium can interfere with the electric field, preventing proper vesicle formation or causing premature vesicle lysis.

Microfluidic System Constraints

Microfluidic approaches face several critical limitations that hinder their broader clinical translation [101]. The difficulty in controlling membrane composition, particularly cholesterol incorporation, represents a fundamental challenge affecting membrane fluidity and stability. Cholesterol distribution within microfluidically generated vesicles often lacks uniformity due to rapid mixing dynamics and limited residence time during assembly [62]. Additionally, residual solvent contamination, batch-to-batch variability, and the

complexity of scaling up production while maintaining vesicle quality pose significant barriers to commercialization [63].

1.5 Characterization Method Limitations

Microscopic Technique Constraints

Despite their widespread application, microscopic techniques face several fundamental limitations that can compromise data interpretation and experimental reproducibility. Given the quite large number of techniques available for investigating model cell membranes, there is no single "recipe for success" readily available when it comes to a specific researcher's experimental needs [102]. AFM, while providing nanometric resolution, requires sample dehydration or fixation that may introduce artifacts and alternative membrane properties. The technique is also limited to surface analysis and cannot provide information about internal membrane dynamics or bulk properties.

Dynamic Light Scattering, despite its utility in size determination, suffers from significant limitations in polydisperse systems and cannot distinguish between different types of particles in mixed populations. DLS is particularly effective for determining vesicle diameters in suspension, although it cannot provide biochemical information or cellular origin data [103]. The technique assumes spherical particle geometry, which may not accurately reflect the morphological diversity of vesicular systems, particularly those undergoing fusion or aggregation processes.

Spectroscopic Method Limitations

Fluorescence-based techniques, while highly sensitive, are inherently limited by photobleaching, phototoxicity, and the need for fluorescent labeling that may perturb natural membrane behavior [104]. FRAP measurements are constrained by the spatial resolution of optical microscopy and cannot accurately assess molecular mobility in highly crowded membrane environments. The technique

also requires relatively high fluorophore concentrations that may alter membrane properties and interfere with physiological processes [105].

FRET analysis faces challenges related to spectral overlap, orientation factors, and the assumption of random molecular orientations that may not hold in ordered membrane domains [106]. The technique requires precise distance measurements that can be affected by conformational changes and environmental factors, leading to potential misinterpretation of molecular interactions.

1.6 Physiological Relevance and Translation Challenges

Model System Oversimplification

No model system will mimic all properties of a natural membrane; however, it has been shown that specific characteristics of a membrane can be simulated very accurately using model systems [107].A fundamental limitation of all membrane model systems is their inherent oversimplification compared to biological membranes. Native cellular membranes contain hundreds of different lipid species, numerous membrane proteins, and complex architectural features such as membrane rafts and cytoskeletal attachments that are difficult to replicate in model systems.

The absence of transmembrane proteins in most vesicular models significantly limits their physiological relevance, as these proteins play crucial roles in membrane permeability, stability, and drug interactions. Additionally, the lack of asymmetric lipid distribution across membrane leaflets, a hallmark of biological membranes, further reduces the predictive power of symmetric model systems.

Scalability and Clinical Translation Barriers

However, there are still some limitations existing in the clinical translation of such research area. As the whole cell delivery system, it's hard for carrier RBC to fulfill the location release except for RES targeting [108]. The translation from laboratory-scale membrane model studies to clinical applications faces numerous challenges. Scale-up manufacturing processes often introduce variability in vesicle properties, affecting reproducibility and batch-to-batch consistency required for pharmaceutical applications.

Regulatory approval processes for membrane-based drug delivery systems are complex and time-consuming, requiring extensive safety and efficacy data that may not directly correlate with model system predictions. The long-term stability of vesicular formulations under storage conditions and the potential for lipid oxidation present additional challenges for commercial viability.

1.6.1 Methodological and Technical Limitations

Standardization and Reproducibility Issues

It is difficult to compare results obtained using different model cell membranes and techniques, and not all in vitro studies translate as well to an estimation of the in vivo biological activity or understanding of mode of action [102]. The lack of standardized protocols across different research groups and institutions leads to significant variability in experimental outcomes and hampers comparative studies. Different laboratories may use varying lipid sources, preparation methods, and characterization criteria, making it challenging to establish universal quality standards.

The temporal stability of membrane models during experiments presents another limitation, as vesicles may undergo fusion, aggregation, or lipid phase transitions that alter their properties over time. This temporal instability can

confound experimental results and limit the duration of studies that can be performed with a given sample.

Analytical Sensitivity and Detection Limits

Many characterization techniques lack the sensitivity required to detect subtle membrane changes induced by pharmaceutical compounds at therapeutically relevant concentrations. Mass spectrometry-based approaches, while highly sensitive, may require sample preparation procedures that disrupt membrane integrity and alter the very interactions being studied [109].

The inability to perform real-time, non-invasive monitoring of drug-membrane interactions in physiologically relevant environments represents a significant analytical gap. Most techniques require either labeling, fixation, or other modifications that may introduce artifacts and limit the physiological relevance of the observations [69].

1.6.2 Environmental and Operational Constraints

pH and Ionic Strength Sensitivity

Membrane model systems are highly sensitive to environmental conditions such as pH, ionic strength, and temperature. Small variations in these parameters can dramatically alter membrane properties and drug interactions, making it difficult to maintain consistent experimental conditions. For instance, the presence of counterions like Na^+ can significantly modify the electrostatic structure of anionic bilayers, affecting binding affinities *[12]*. Additionally, the buffering capacity of model systems may not accurately reflect the complex ionic environment of biological fluids.

Storage and Handling Limitations

Vesicular systems suffer from limited shelf-life and require specific storage conditions to maintain integrity. Freeze-thaw cycles, osmotic shock, and

mechanical stress during handling can compromise vesicle structure and affect experimental reproducibility. The need for freshly prepared samples increases experimental costs and limits the feasibility of large-scale studies, as extensive protocols are often required to ensure entrapment efficiency and stability over time [46].

1.6.3 Future Directions and Emerging Solutions

Advanced Model System Development

Recent advances in microfluidic technology and 3D bioprinting offer promising approaches for creating more physiologically relevant membrane models [4]. The development of hybrid systems that combine synthetic and biological components may address some current limitations while maintaining experimental control.

Integration of artificial intelligence and machine learning approaches for data analysis and prediction may help overcome some of the interpretive challenges associated with complex membrane interactions [20]. These computational tools could potentially identify patterns and relationships that are not apparent through traditional analytical approaches.

Regulatory and Standardization Initiatives

The establishment of international standards for membrane model characterization and validation would greatly enhance the reproducibility and clinical relevance of research findings. Collaborative efforts between academic institutions, pharmaceutical companies, and regulatory agencies are needed to develop consensus protocols and quality criteria.

Investment in advanced analytical techniques that can provide real-time, non-invasive monitoring of membrane processes under physiological conditions will be crucial for bridging the gap between model systems and biological reality

[6]. These developments should focus on maintaining the native state of membrane systems while providing sufficient analytical sensitivity and specificity.

The continuous evolution of membrane model systems, despite their current limitations, remains essential for advancing pharmaceutical sciences and developing next-generation therapeutic strategies. Addressing these challenges through interdisciplinary collaboration and technological innovation will be crucial for realizing the full potential of membrane-based drug delivery and discovery approaches.

CHAPTER 2

General Objectives

The main objective of this work is to develop an integrated and modular experimental platform to streamline the production and analysis of lipid-based systems, with particular focus on Giant Unilamellar Vesicles (GUVs) and Langmuir–Blodgett techniques. The project is conceived to simplify laboratory workflows, reduce manual intervention, and increase the volume of data generated per unit time, enabling seamless integration with proprietary artificial intelligence tools developed by SoftMining. SoftMining is an Italian company specialized in computational chemistry and artificial intelligence for drug discovery and biomaterials. Its interest in biological membranes and lipid systems reflects the need to validate predictive models with experimental evidence. In this context, studies on Giant Unilamellar Vesicles (GUVs) and Langmuir–Blodgett monolayers provide quantitative data on membrane organization, dynamics, and molecular interactions, thereby affirming and refining the company's computational predictions.

To achieve this, a Langmuir balance system was designed using Arduino-based hardware, chosen for its modularity, affordability, and ease of customization. The system supports all standard functionalities of Langmuir and Langmuir–Blodgett experiments, including surface pressure monitoring, lateral barrier control, and a secondary vertical dipping axis for lipid deposition on solid substrates. A dedicated software interface was developed to provide full control over experimental parameters, protocol execution, and real-time data acquisition.

In parallel, a custom electroformation cell for GUV production was engineered to ensure reproducibility, compatibility with fluorescence-based assays, and adaptability to automated workflows. The system includes a stoichiometric calculation tool that automatically computes the required lipid molar quantities for electrode deposition, based on user-defined geometries and concentrations, minimizing human error and preparation time.

To support high-throughput experimentation, a data management framework was implemented to aggregate, structure, and annotate experimental outputs, facilitating batch processing and standardized formatting for downstream analysis. This infrastructure is designed to interface directly with machine learning pipelines, enabling rapid extraction of meaningful patterns from large datasets.

Complementing the hardware and data infrastructure, a spectral deconvolution module was developed to process fluorescence emission spectra from vesicle-based assays. The tool performs automatic peak identification and grouping, generating concise analytical reports with minimal user input, thereby accelerating post-experimental interpretation.

Overall, this work aims to provide a flexible and scalable platform for membrane biophysics, enhancing experimental efficiency and data accessibility while laying the groundwork for AI-assisted discovery in lipid research.

CHAPTER 3

Arduino-based Langmuir Blodgett trough

3.1 Introduction

The Langmuir–Blodgett (LB) technique is a foundational method for the controlled deposition of amphiphilic molecules at the air–water interface, enabling the formation of monolayer and multilayer films with nanometric precision. These films are widely employed in materials science, surface engineering, biosensing, and molecular electronics due to their tunable structural and functional properties[110].

Despite its versatility, the adoption of LB technology in smaller laboratories remains limited by the high cost and proprietary nature of commercial systems. Standard LB balances typically range from €20,000 to €50,000 [111], placing them beyond the reach of many academic and early-stage research environments. Moreover, their closed architecture often restricts hardware and software customization, impeding experimental innovation and integration with emerging technologies.

To address these limitations, this project introduces a fully modular LB balance system based on the Arduino microcontroller platform. Arduino's open-source ecosystem offers a robust foundation for building cost-effective, customizable instrumentation [112]. By leveraging compatible sensors, actuators, and expansion modules, the system achieves precise control over surface pressure, barrier movement, and vertical dipping—core functionalities required for Langmuir and Langmuir–Blodgett experiments.

The open architecture of the Arduino platform facilitates seamless integration with external devices and software environments, enabling real-time data acquisition, automated protocol execution, and feedback-controlled experimentation [113]. This flexibility supports the development of advanced

experimental workflows, including coupling with fluorescence imaging, spectroscopic analysis, and machine learning-based data interpretation.

Importantly, the system is designed to be adaptable to diverse research needs. Its modular structure allows for straightforward upgrades, such as the addition of a second vertical axis for lipid transfer onto solid substrates, or the implementation of custom sensors for environmental monitoring. The collaborative nature of open-source development further encourages the dissemination and refinement of design files, firmware, and analytical tools, fostering a community-driven approach to instrumentation innovation.

This chapter presents the design rationale, implementation details, and validation results of the Arduino-based LB balance. Technical specifications are discussed in relation to commercial benchmarks, and potential modifications are outlined to illustrate the system's scalability. The findings demonstrate that open-source hardware can provide a viable and powerful alternative to proprietary LB systems, particularly in contexts where affordability, adaptability, and data integration are critical.

3.1.1 Original Contribution and Rationale

While commercial Langmuir-Blodgett troughs are established tools in interface science, their widespread adoption is often hindered by prohibitive costs and proprietary, closed-source ecosystems. The original contribution of this doctoral work lies in the complete re-engineering of this instrumentation using accessible, off-the-shelf components (Arduino architecture, 3D printing) without compromising analytical sensitivity.

A direct comparison with market standards highlights the impact of this approach. While entry-level commercial systems (e.g., KSV NIMA or Kibron) typically range from €15,000 to €25,000, the total bill of materials (BOM) for our custom device remains below €500. This drastic reduction effectively democratizes access to advanced membrane biophysics, enabling smaller

laboratories to perform high-precision surface analysis. Furthermore, unlike commercial "black boxes" where proprietary software prevents user intervention, our Python-based control suite (LanGUImuir) offers full transparency. This open-source architecture allows researchers to implement novel compression profiles (e.g., oscillating barriers for rheology) and integrate raw data directly into custom analysis pipelines, capabilities often precluded in standard commercial packages. Despite the significant cost reduction, the core metrological characteristics are comparable to industry standards. Thanks to the integration of a 24-bit acquisition system, the device achieves a force sensor resolution of ±0.1 mN/m and high barrier positioning accuracy, as demonstrated by the validation isotherms (see Section 3.9-3.10). The primary trade-off lies in the requirement for manual assembly and the absence of integrated temperature control modules, which are standard in high-end units but can be added modularly in our design.

Crucially, the open hardware architecture provides a modular foundation for future upgrades. The microcontroller retains sufficient I/O capacity to integrate supplementary metrological tools without altering the core system. Future implementations could include a computer vision module for dynamic contact angle goniometry during dipping cycles, or a Kelvin probe to monitor surface potential. The latter would provide complementary data on molecular orientation and dipole moments, transforming the device into a multimodal analysis platform capable of correlating thermodynamic phase changes with structural reorganization.

3.2 Design and functional overview

The Langmuir–Blodgett balance developed in this work is designed to measure the surface pressure exerted on an inert sheet partially immersed in a liquid subphase, typically water. The system is controlled via an Arduino microcontroller, which orchestrates all core functionalities, including barrier

movement, force acquisition, and substrate dipping. The platform supports multiple operational modes:

- Taring the balance
- Moving the lateral barriers
- Measuring the force applied to the Wilhelmy plate
- Managing data in mV/V or N/m
- Dipping a solid substrate into the phospholipid monolayer while moving the lateral barriers

These features are implemented using open-source libraries such as "*ezButton"*, "*AccelStepper*", and "*HX711*", which provide robust control over limits management, stepper motor dynamics, and load cell signal amplification, respectively.

3.3 Hardware components

In line with the project's emphasis on modularity and accessibility, the system integrates a selection of carefully chosen components, each fulfilling a specific operational role. The design prioritizes modularity, affordability, and compatibility with open-source control protocols, allowing for seamless customization and future expansion. Below is an overview of the key elements and their respective functions within the system architecture.

- Load Cell and HX711 Amplifier:

A Forsentek 30 g load cell is employed to detect the force exerted on the Wilhelmy plate. The HX711 amplifier, specifically designed for load cell applications, ensures high-resolution analog-to-digital conversion, enabling precise surface pressure measurements.

- Barriers:

The compression barriers are fabricated from polytetrafluoroethylene (PTFE), selected for its low friction coefficient and chemical inertness. These properties ensure smooth, reproducible movement during monolayer compression.

- Microcontroller:

An Arduino board serves as the central control unit, managing motor operations, force acquisition, and serial communication with the user interface. This configuration eliminates the need for dedicated display hardware, reducing system complexity and cost.

- Motor Control:

Stepper motors are driven via dedicated drivers, allowing for precise barrier positioning. The system is built to support both active and passive compression modes, with or without concurrent force measurement, offering flexibility in experimental design.

- Power Supply:

A regulated power source ensures stable operation of both the Arduino and the HX711 module. Voltage compatibility is maintained across all components to prevent signal drift and ensure measurement consistency.

3.4 Measurement principle

Surface pressure is quantified using the Wilhelmy plate method, wherein a thin plate is suspended vertically and partially immersed in the subphase [114, 115]. The net downward force F acting on the plate is given by:

$$F = \rho_l * gl_p * w_p * t_p + 2\gamma(t_p + w_p) * Cos\theta - \rho_l * gt_l * w_l * h_l$$

Equation 1 *describes the vertical force balance on the plate: the gravitational force (weight), the downward pull of surface tension along the perimeter, and the upward buoyancy force from the displaced liquid.*

Where:

- ρ is the material density.
- g is the gravitational acceleration.
- l, w, t are the length, width, and thickness of the plate, respectively.
- γ is the surface tension.
- θ is the contact angle.

The surface pressure π is defined as the reduction in surface tension of the pure subphase (γ_0) caused by the presence of the monolayer (γ). It is determined by measuring the change in force ΔF acting on the plate [115] :

$$\pi = -\Delta\gamma = -\left[\frac{\Delta F}{2\left(w_p + t_p\right)}\right]$$

Equation 2 *defines surface pressure π based on the force change ΔF. Assuming complete wetting (θ =0°) and constant buoyancy, the measured force variation is directly proportional to the reduction in surface tension*

For thin plates where $w_p \gg t_p$, this simplifies to [116]:

$$\pi = -\Delta F / 2w_p$$

Equation 3 *For thin plates (w≫t), the perimeter is approximated as 2w. This simplification streamlines real-time calculations without introducing significant experimental error.*

3.5 Isotherm Acquisition

Surface pressure–area isotherms are obtained by compressing the monolayer at a constant rate while continuously monitoring the surface pressure. The resulting curve reveals distinct phase transitions—gaseous (G), liquid-expanded

(L_1), liquid-condensed (L_2), and solid (S)—each corresponding to specific molecular packing states at the interface.

3.6 Implementation and modularity

The Arduino firmware is programmed to interpret serial commands, execute motor movements, and transmit measurement data, such as pressure on the plate, and position of the barriers. The system includes a taring function to zero the balance prior to each experiment, and supports periodic calibration to maintain accuracy.

The modular architecture allows for future expansion, including the integration of a second vertical axis for substrate immersion during Langmuir–Blodgett deposition, or the addition of different kind of sensors. This design philosophy ensures compatibility with evolving experimental needs and facilitates the incorporation of additional sensors or actuators.

For the housing of the different modules I developed a dedicated circuit on a perfboard, that holds the different section dedicated to movements and measurements. There is space for future upgrades that may include environmental monitoring modules, to maintain optimal conditions during monolayer compression and transfer, and automated cleaning and calibration routines, reducing operator intervention and improving reproducibility across multiple experimental cycles.

The firmware is designed to support event-driven programming, enabling asynchronous execution of barrier movement and force acquisition tasks. This approach minimizes latency during isotherm acquisition and ensures accurate synchronization between mechanical operations and data logging.

To enhance scalability, the hardware layout adopts a modular PCB design, where individual functional blocks—motor drivers, signal amplifiers, and communication interfaces—are mounted on detachable boards. This

configuration simplifies maintenance and allows rapid replacement or upgrade of components without redesigning the entire system.

Finally, the open-source nature of the platform encourages collaborative development. Design files, firmware, and control scripts can be shared within the scientific community, promoting iterative improvements and fostering the creation of advanced features such as AI-assisted surface pressure prediction or adaptive compression algorithms based on real-time feedback.

3.7 Circuit design and functional overview

The Langmuir–Blodgett trough control system is based on an ATmega2560 microcontroller, selected for its high I/O availability and compatibility with open-source development environments. The circuit integrates three main functional blocks:

Force Measurement Module

A Forsentek 30 g load cell is connected to an HX711 precision amplifier, enabling high-resolution analog-to-digital conversion for surface pressure measurements via the Wilhelmy plate method. The HX711 communicates with the microcontroller through a two-wire interface (PD_SCK and DOUT), ensuring minimal noise and accurate force acquisition.

Motion Control Subsystem

The lateral barriers and vertical dipping axis are actuated by stepper motors driven by A3967 EasyDriver modules. Each driver supports microstepping and adjustable current control via LM317-based voltage regulators, allowing fine-tuned torque and smooth motion. Limit switches on both X and Y axes provide positional feedback and safety during automated compression cycles.

Power and Communication Infrastructure

The system is powered through a DC input (12 V), that feeds directly the motor drivers, and that is regulated to 5 V for logic and 3.3 V for auxiliary components. The Arduino CH340G USB-to-serial converter ensures seamless communication with the external Python-based control interface. Additional passive components (resistors, capacitors, inductors) stabilize the power supply and filter signal noise, while LEDs provide visual feedback for operational states.

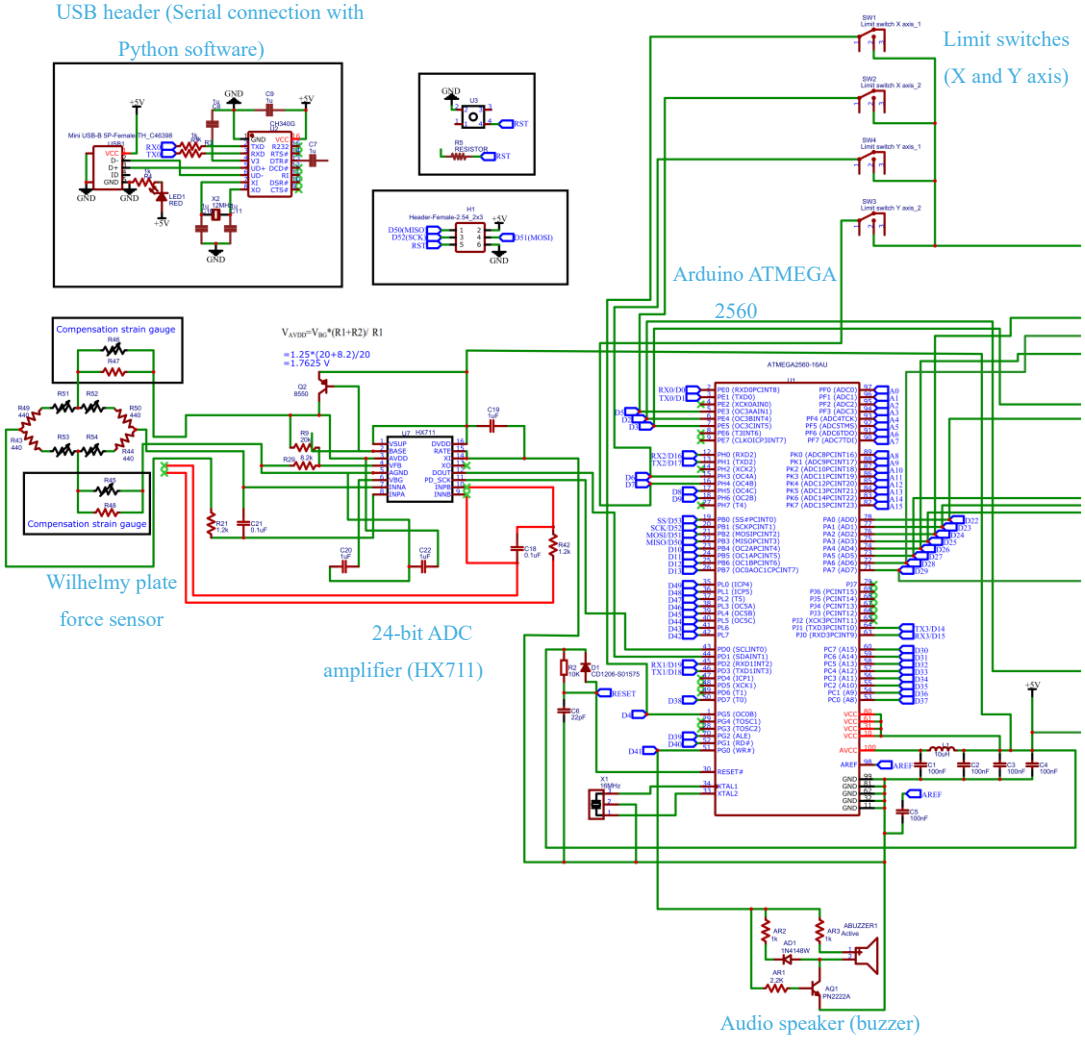
USB header (Serial connection with Python software)
Limit switches (X and Y axis)
Arduino ATMEGA 2560
Wilhelmy plate force sensor
24-bit ADC amplifier (HX711)
Audio speaker (buzzer)

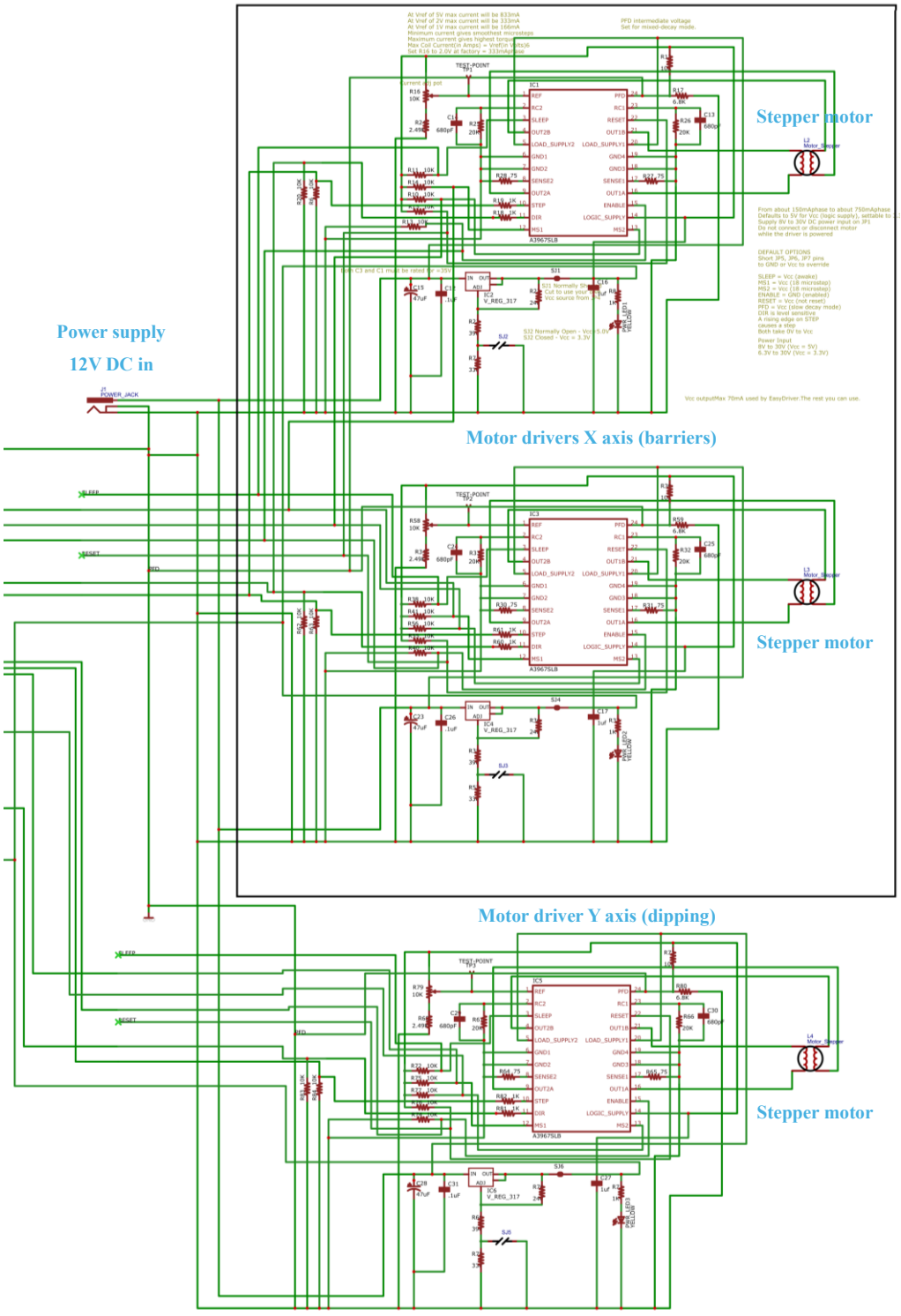

Figure 7 *Complete circuit schematic of the Langmuir-Blodgett control unit. The system is centered around an* ***ATmega2560 microcontroller****, and includes the force measurement interface using an HX711 24-bit ADC; the motion control subsystem with A3967 EasyDrivers for X (barrier) and Y (dipping) stepper motors; mechanical limit switches for safety and positional feedback.*

The modular architecture allows future expansion, including additional sensors for environmental monitoring or integration with optical devices. Figure 8 illustrate the complete schematic, highlighting the interconnections between the microcontroller, load cell amplifier, motor drivers, and peripheral components; Figure 8 shows two iterations of the modular prototype.

a) b)

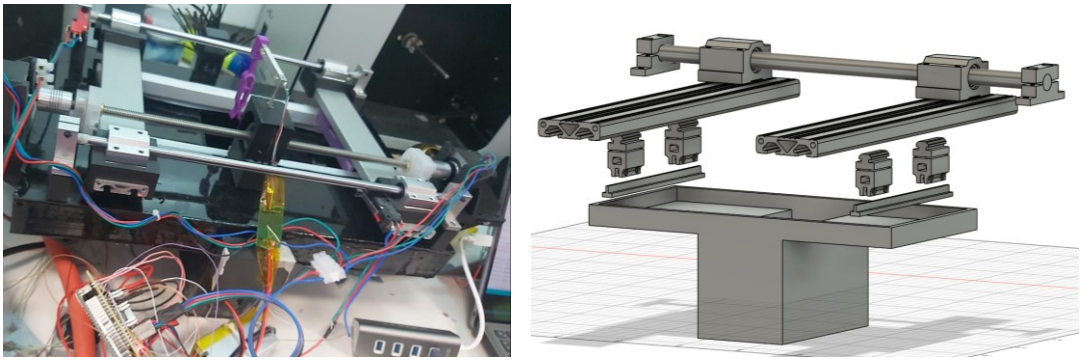

Figure 8 *a) First working prototype of Arduino-based Langmuir trough; b) exploded view of second prototype*

3.8 Firmware architecture

The firmware was developed to ensure precise control of the Langmuir–Blodgett trough operations, including surface pressure acquisition, barrier movement, and substrate dipping. The architecture follows a modular design, enabling easy maintenance and future upgrades. The main functional blocks are:

Core Modules

1 Initialization

- Configure microcontroller pins for sensors, actuators, and communication.
- Initialize libraries for stepper motor control, load cell reading, and serial communication.
- Perform system calibration (tare load cell, set barrier home position).

2 Main Loop

- Continuously monitor user commands received via serial interface.

- Execute corresponding routines (e.g., start compression, acquire isotherm, dip substrate).
- Update real-time data to the host computer.

3 Safety and Error Handling

- Monitor limit switches to prevent mechanical overtravel.
- Implement emergency stop on critical errors (e.g., sensor failure, communication timeout).

Pseudocode

```
BEGIN
    // --- Setup Phase ---
    Initialize Serial Communication (baud = 115200)
    Initialize HX711 for load cell
    Initialize Stepper Drivers (X-axis, Y-axis)
    Configure Limit Switches
    Tare Load Cell
    Home Barriers and Vertical Axis

    // --- Main Loop ---
    WHILE system is ON:
        IF Serial Command Received:
            Parse Command
            SWITCH (Command):
                CASE "TARE":
                    Tare Load Cell
                CASE "MOVE_X":
                    Move Barrier to Target Position
                CASE "MOVE_Y":
                    Move Vertical Axis to Target
Position
                CASE "READ_FORCE":
                    Read HX711 Value
                    Convert to Surface Pressure
                    Send Data to Host
                CASE "RUN_ISOTHERM":
                    Execute Compression Protocol:
                        FOR area in defined range:
                            Move Barriers incrementally
                            Read and log surface
pressure
                CASE "STOP":
                    Halt all movements
        END SWITCH

        // Safety Checks
```

```
        IF Limit Switch Triggered:
            Stop Motor
            Send Alert to Host
    END WHILE
END
```

Full implementation available under the MIT license on GitHub at:

https://github.com/DavideRmni/Trough_firmware

3.9 Software interface

To complement the hardware automation, a dedicated control software was developed in Python. The development process followed an iterative approach, resulting in three major revisions, each introducing new functionalities to address specific experimental needs.

Objectives

The primary goals of the software are:

- Reliable Communication with the Arduino firmware via serial protocol.
- Experiment Automation, including script execution and timed operations.
- Real-Time Visualization of surface pressure and barrier position.
- Data Management, enabling comprehensive logging and export in standard formats.
- Error Handling and Debugging to ensure operational safety and reproducibility.

Development Process

The development process followed an iterative approach, resulting in three major revisions:

1 First Version – Command-Line Interface

The first iteration of a graphical interface for the trough (Figure 9) was a text-based interface designed to establish basic serial communication with the Arduino firmware. It allowed for the exchange of low-level commands (e.g., barrier movement steps) and simple data logging. While functional for preliminary testing, the lack of real-time visualization made it difficult to monitor the experiment's progress and detect mechanical anomalies instantly.

Figure 9 *First version of graphical interface for the LanGUImuir*

2 Second Version – Graphical User Interface (GUI)

To improve usability, the second iteration (Figure 10) introduced a real time plotting built with the Tkinter library. This version represented a significant leap forward, incorporating:

- **Real-time Plotting**: A dynamic graph to visualize surface pressure trends during compression.
- **Script Management**: A dropdown menu system to load and execute pre-written compression protocols (text files).

- **Timers**: Integrated countdowns to synchronize manual operations (e.g., lipid deposition) with the automated script.

Figure 10 *Second version of the graphical interface for the control of the Langmuir Trough*

4 Third Version – Final Release

The final version, named LanGUImuir (Figure 11 and 12), was developed to provide full experimental control and robust error handling. In addition to the features of Version 2, it introduced:

- **Manual Controls:** A dedicated control panel enables the independent movement of lateral barriers and the substrate dipping mechanism (Z-axis). This feature is essential for precise initial positioning and for executing cleaning protocols without running full automation scripts.
- **Dual Data Representation:** The interface provides simultaneous visualization of sensor data in both raw units (mV/V, representing the raw sensor output) and physical units ($N \cdot m^{-2}$ or mN/m, representing converted surface pressure). This dual display allows the user to monitor physical phenomena while keeping track of sensor health and drift.

- **Debug Mode:** A dedicated debugging console was integrated for troubleshooting and error management. This mode exposes the raw serial traffic and internal error flags, facilitating immediate diagnosis of communication issues or hardware faults during experiments.
- **Flexible Data Export:** The data management module was overhauled to allow users to save either the complete machine interaction log (for auditing purposes) or only the processed experimental data in CSV format, ensuring compatibility with downstream analysis software.This progressive evolution reflects the transition from a minimalistic command-driven tool to a comprehensive, user-friendly platform capable of supporting complex experimental workflows. The modular design ensures compatibility with future upgrades, including integration with machine learning algorithms for predictive control and automated data interpretation.

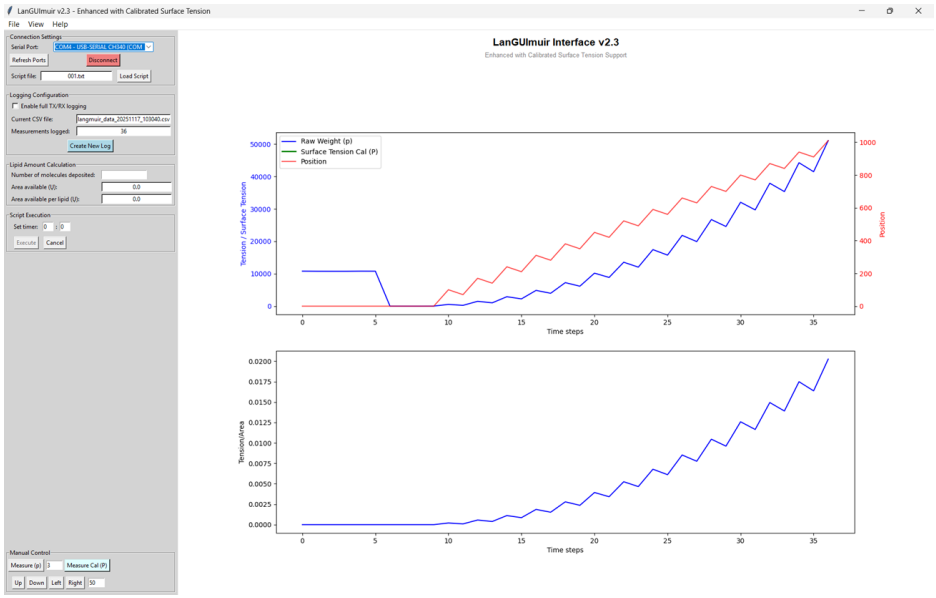

Figure 11 *The final LanGUImuir interface, showing the manual control panel and real-time isotherm visualization*

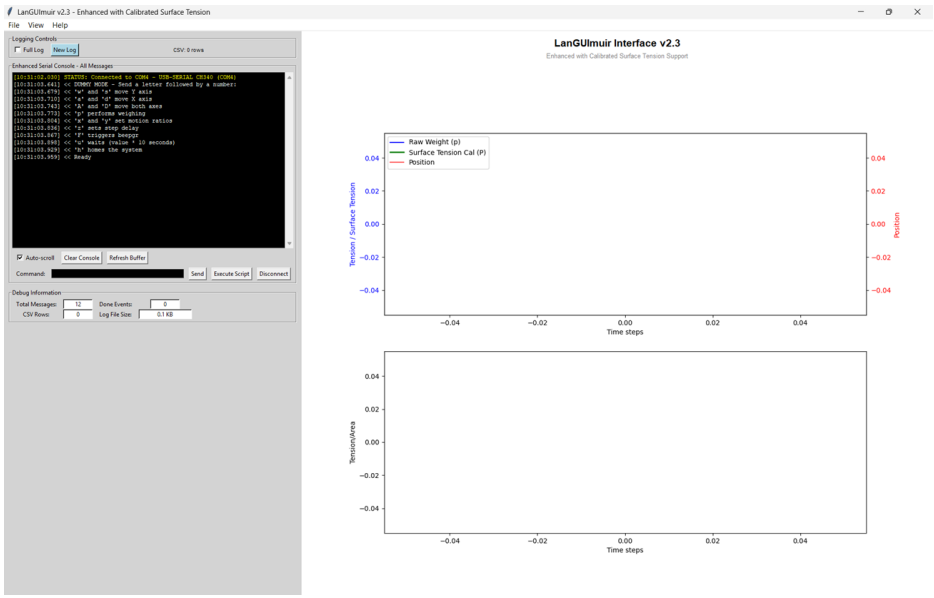

Figure 12 *The final LanGUImuir interface, showing real-time isotherm visualization and debug window*

This mature version serves as the primary tool for all data acquisition presented in this thesis. The logic governing the final interface is summarized in the pseudocode below.

Pseudocode of the final version

```
BEGIN
    Initialize application:
        - Create main window (Tkinter)
        - Setup frames: Controls (left), Plots (right)
        - Initialize managers:
            • LoggingManager (CSV + full log)
            • SerialManager (serial communication)
            • DataProcessor (measurement handling)
            • ScriptExecutor (script automation)

    Setup GUI components:
        - Connection settings (port selection,
connect/disconnect)
        - Script loading and execution (with timer)
        - Logging configuration (CSV and full TX/RX)
        - Lipid calculation panel (area per molecule)
        - Manual controls (measure, calibrated measure,
move axes)
         - Debug mode (serial console, message buffer,
stats)
        - Plot area (real-time graphs for weight, surface
tension, position)
```

```
    Main event loop:
        WHILE application is running:
            - Update GUI elements periodically
            - Read data from serial queue:
                IF message type == "rx":
                    Process message:
                        • Extract weight or surface
tension
                        • Update buffers and moving
average
                        • Log to CSV
                IF message type == "tx" or "status":
                    Update console display
                IF message type == "error":
                    Show error in console
            - Update plots:
                • Plot raw weight (blue)
                • Plot calibrated tension (green)
                • Plot barrier position (red)
                • Plot tension/area curve
            - Refresh logging info and debug statistics

    Script execution:
        - Load script file
        - Optional delay before start
        - Send commands sequentially to Arduino
        - Wait for "Done" or timeout
        - Log execution status
        - Allow cancellation

    Manual commands:
        - Send single commands for measurement or
movement
        - Track command type ('p' raw, 'P' calibrated)

    On exit:
        - Close serial connection
        - Flush and close log files
END
```

Full implementation available on GitHub at

https://github.com/DavideRmni/LanGUImuir under the MIT License.

Integration and Scalability

The modular architecture of the Python interface facilitates future upgrades, including:

- Integration with machine learning algorithms for predictive control.
- Automated data interpretation and anomaly detection.
- Compatibility with additional sensors and experimental modules.

Overall, the software interface represents a critical component of the experimental platform, bridging hardware automation with advanced data analytics and user-centric design.

3.10 Signal-to-Noise Ratio (SNR)

The signal-to-noise ratio (SNR) is a critical parameter for evaluating the reliability of surface pressure measurements during Langmuir–Blodgett experiments. A high SNR ensures that the recorded data accurately reflects monolayer behavior without being significantly affected by electronic or environmental noise. This analysis was performed to validate the performance of the Arduino-based trough and its associated acquisition system under realistic experimental conditions.

3.11 Experimental Setup

Measurements were performed under static conditions, without barrier compression, to isolate the effect of the surfactant on the Wilhelmy plate response. Two sets of readings, shown in table 1 and graph 1, were collected:

- Control (Water): Baseline measurements in pure water.
- Test (SLES): Measurements after introducing 100 µL of a SLES solution at 8.67×10^{-4} M onto the aqueous subphase.

Each dataset consisted of ten consecutive raw readings, expressed in counts, recorded under identical environmental conditions. The difference between the two sets was calculated relative to the mean of the control group to highlight the magnitude of the signal shift induced by the surfactant.

	Water	SLES	Difference
	886732.69	882923.00	-3776.04
	886706.00	882912.31	-3786.73
	886729.00	882966.31	-3732.73
	886728.00	882918.69	-3780.35
	886696.69	882839.31	-3859.73
	886722.31	882847.69	-3851.35
	886697.00	882844.00	-3855.04
	886657.31	882838.00	-3861.04
	886665.69	882762.31	-3936.73
	886655.69	882754.00	-3945.04
Average	886699.04	882860.56	-3838.48
St.dev	30.186572	69.56	
Min	886655.69	882754.00	-3945.04
max	886732.69	882966.31	-3732.73

Table 1 *Comparison of raw sensor readings (ADC counts) with water and SLES solution*

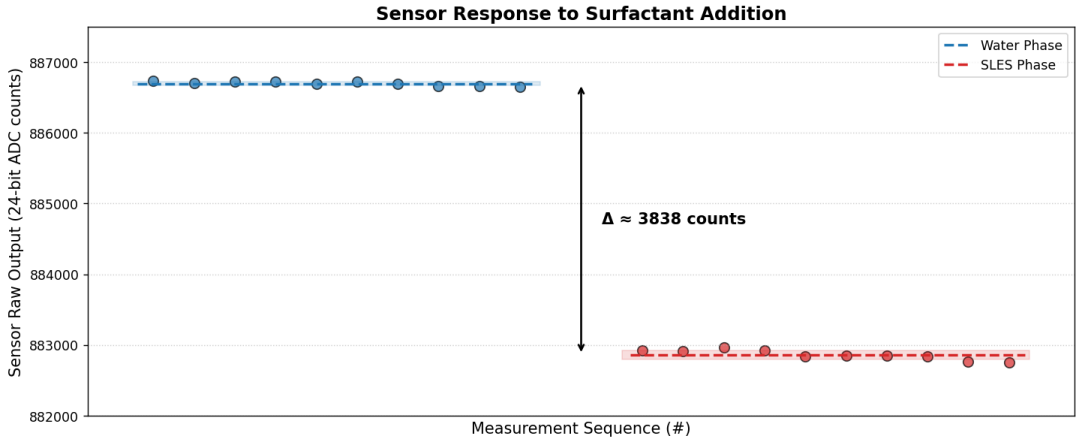

Graph 1 *Real-time sensor response before and after the addition of Sodium Laureth Sulfate (SLES). The plot displays the raw digital output from the 24-bit ADC expressed in counts, where 1 count corresponds to the Least Significant Bit (LSB) of the acquisition system The measurements exhibit a stable baseline in water (blue circles) followed by a distinct signal shift upon surfactant addition (red circles). Dashed lines represent the mean value for each phase, while the shaded regions indicate Standard Deviation. The system demonstrates a high sensitivity with a clear signal shift ($\Delta \approx 3840$ counts) and a negligible noise floor ($\sigma_{water} \approx 30$ counts) , confirming the capability to detect subtle surface tension variations.*

3.11.1 SNR calculation

To quantify the reliability of the measurement system under static conditions, the signal-to-noise ratio (SNR) was computed using the mean difference between the two datasets as the signal and the standard deviation of the control group as the noise component. The formula applied was:

$$SNR(db) = 20\log_{10}\left(\frac{Signal}{Noise}\right)$$

Equation 4 *Signal-to-Noise Ratio equation*

where:

- **Signal** = average difference between the "Water" and "SLES" readings = 3838.48 counts
- **Noise** = standard deviation of the control group = 30.19 counts

Substituting these values:

$$SNR(db) = 20\log_{10}\left(\frac{3838.48}{30.19}\right) \approx 42.1db$$

Equation 5 *Signal-to-Noise equation applied to preliminary data*

This result indicates a high signal-to-noise ratio, confirming that the system can reliably detect the effect of introducing surfactants on the Wilhelmy plate response, under static conditions without barrier compression.

3.11.2 Dynamic response to surfactants

To validate the system's capability to detect surface tension modifications, a series of tests were conducted using anionic surfactants. These experiments aimed to assess both the static sensitivity limit, detecting the immediate presence of surface-active agents, and the dynamic response during barrier compression.

Sensitivity Assessment

Initial validation was performed under static conditions to quantify the load cell's response to a drastic change in surface tension. A baseline measurement was established with pure deionized water, followed by the addition of a surfactant solution (SLES). As detailed in Table 1, the introduction of the surfactant induced a significant shift in the raw sensor output. The differential analysis between the "Water" and "SLES" states revealed an average deviation of approximately 3,838 counts. Based on the system's characterization, this corresponds to a net force variation (ΔF) of approximately 1.03 mN (0.105 gf). This result confirms that the hardware resolution is sufficient to detect surfactant adsorption at the air-water interface even in the absence of compression.

Sensitivity and Dynamic Response to Surfactants

To quantify the instrument's limit of detection and validate its response to dynamic changes, a series of tests were conducted using Sodium Laureth Sulfate (SLES), a standard anionic surfactant. The objective was to verify the system's ability to track the reduction in surface tension during barrier compression.

Experimental Setup

Validation was performed by depositing 100 µL SLES solution (8.67×10^{-4} M) onto the aqueous subphase. After an equilibration period, a compression script was executed to reduce the available surface area while synchronously logging the force exerted on the Wilhelmy plate.

Results

As illustrated in Graph 2, the system successfully recorded the correlation between barrier position and the raw force signal. The graph exhibits two distinct trends:

1 **Barrier Movement** (Orange Line): The stepper motors advanced linearly from position 0 to 16,000 steps, progressively reducing the trough area.

2 **Force Response** (Blue Line): The raw sensor reading initially remained stable but subsequently exhibited a monotonic decrease as compression advanced.

This downward trend in the raw signal is physically consistent with the Wilhelmy plate principle: as the surfactant monolayer is compressed, the surface pressure (Π) increases, causing a corresponding reduction in surface tension (γ). Since the downward force acting on the plate is proportional to γ, the measured weight decreases. This dynamic correlation validates the effectiveness of the control logic in synchronizing the mechanical actuation with the HX711 acquisition module.

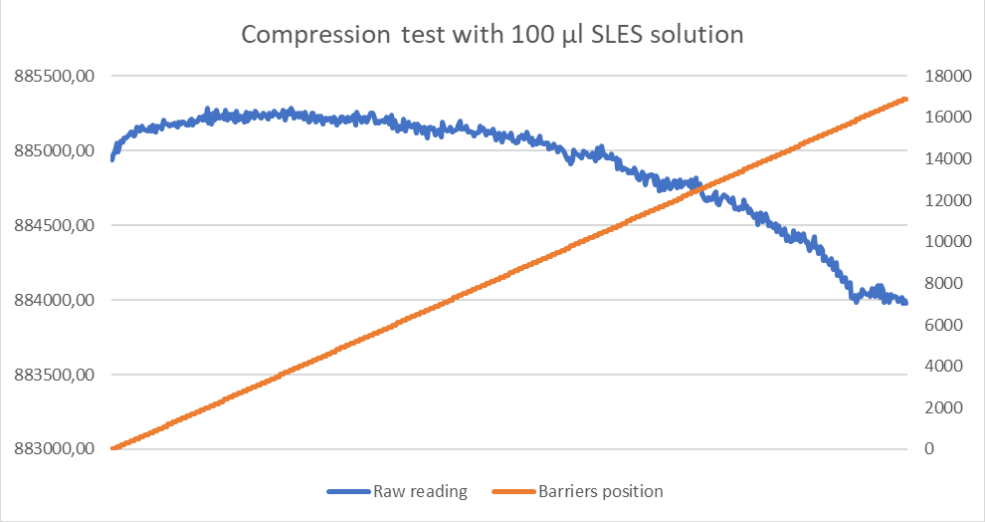

Graph 2 *Dynamic response during the compression of a SLES monolayer (100 µL). The secondary axis (orange) tracks the linear displacement of the barriers (closing), while the primary axis (blue) displays the raw sensor output. The decrease in the measured value corresponds to the reduction in surface tension induced by the monolayer compression.*

3.11.3 Dynamic response to phospholipids

Following the validation with synthetic surfactants, the system was challenged with a complex biological sample to assess its performance in generating pressure-area (Π-A) isotherms.

Sample Specifications

Isotherm acquisition was performed using a mixed phospholipid solution derived from dry egg yolk extract. The lipid composition was characterized as Phosphatidylcholine (PC) 58%, Sphingomyelin (SM) 27%, and Dilauroylphosphatidylethanolamine (DLPE) 15%.

For the experiment, 80 μL of the phospholipid solution (3.63×10^{-8} M) were deposited dropwise onto the aqueous interface.

Experimental Protocol and Phase Transition Detection

Prior to lipid deposition, a standard surface cleaning protocol was applied to ensure a contaminant-free interface. This routine involved repeated compression-expansion cycles combined with surface aspiration to remove any residual impurities from the aqueous subphase. Once the clean baseline was established, the lipid solution was deposited, and the solvent was allowed to evaporate. Subsequent compression cycles successfully resolved the characteristic features of the phospholipid monolayer. As shown in Graph 3, the system tracked the transition from the gaseous/liquid-expanded phase to the Liquid-Solid (LS) transition phase. Although minor environmental noise is detectable, the signal quality remains well within acceptable limits for physicochemical characterization, allowing for a clear distinction of the phase behavior. Consequently, the reliable detection of the condensed phase confirms the trough's capability to compress biological monolayers up to high packing densities.

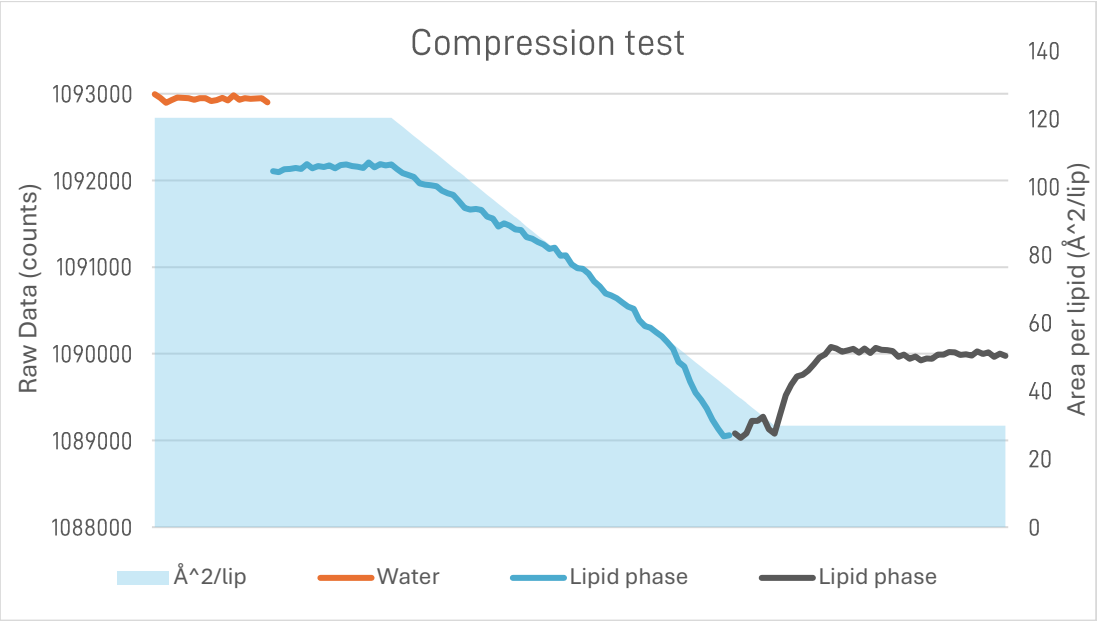

Graph 3 *Compression isotherm of egg yolk phospholipids 80 µL - 3.63 × 10-8 M. The plot displays the raw sensor output (counts) versus barrier compression. The segmented lines (light blue) highlight distinct phase behaviors and changes in monolayer elasticity, indicating stable compression within each phase region.*

3.12 Validation

To validate the trough's performance and the sensitivity of the custom pressure sensor with multicomponent lipid systems, the compression isotherm of egg yolk presented in Section 3.11 (graph 3) was benchmarked against established literature profiles. Figure 13 illustrates a direct comparison between our experimental data and the reference isotherm reported by Mitsche et al.[117].

The recorded isotherm exhibits a smooth, monotonic increase in surface pressure without distinct phase transition plateaus. This behavior is characteristic of natural Egg PC, which typically exists in a **liquid-expanded (LE) state** at room temperature due to the heterogeneity of its acyl chains and the steric hindrance of unsaturated fatty acids [117, 118].

a) b)

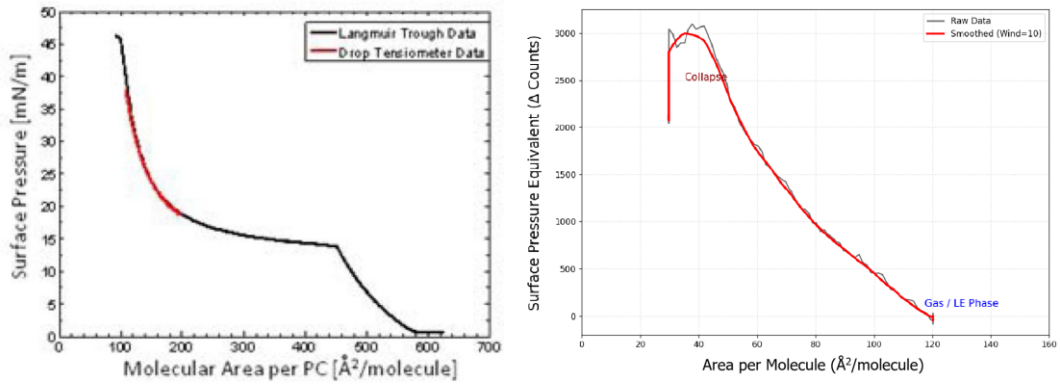

Figure 13 *Benchmarking of the experimental setup against literature data. a) Reference isotherm from Mitsche et al.[117], b) Compression isotherm of egg yolk recorded with the custom-built trough (experimental data from Section 3.11). The comparison highlights the consistency in the monolayer behaviour, characterized by a smooth compression profile and a similar collapse pressure, validating the accuracy of the sensor for complex mixtures.*

Quantitative analysis of the curve reveals a lift-off area (onset of surface pressure) of approximately 100–110 Å^2/molecule, followed by a continuous compression phase. This profile is consistent with standard isotherms reported by Lintker et al., where pure Egg PC monolayers demonstrate a similar expanded behavior compared to sterol-containing mixtures.

Furthermore, the monolayer remains stable up to high compression densities, reaching a collapse point at a limiting molecular area of approximately 45–50 Å^2/molecule. These values align well with the structural parameters reported by Marsh et al., confirming that the recorded signal accurately reflects the physical state of the monolayer [119].

3.13 Auxiliary Tools: The Scriptmaker Utility

To streamlined the experimental workflow and eliminate syntax errors during protocol definition, a companion utility named ScriptMaker was developed. While the initial prototype relied on a command-line interface, the final version

features a full Graphical User Interface (GUI) built with Tkinter, designed to guide the user through the visual construction of valid experiment files.

Interface and Core Functionalities

As shown in Figure 14, the application provides a structured environment for protocol design, implementing the following logic:

- Initialization Options: Simple checkboxes allow the user to automatically inject setup routines—specifically homing (h1) and taring (t3)—at the beginning of the script sequence.
- Command Sequence Management: Users can build a sequence of actions (e.g., "Measure", "Close Barriers") using a dedicated input field. The GUI allows for the dynamic reordering (Move Up/Down) or removal of commands within the list.
- Loop Generation: A specific "Repetitions" field enables the definition of loops (e.g., repeating a compression-measurement cycle N times), automating complex repetitive tasks without manual code duplication.
- File Management: The tool supports both the generation of new files and the appending of commands to existing scripts, with intelligent checks to prevent redundant initialization commands.

Logic Overview

The underlying algorithm ensures that the user's visual inputs are translated into a syntactically correct stream of commands compatible with the LanGUImuir parser.

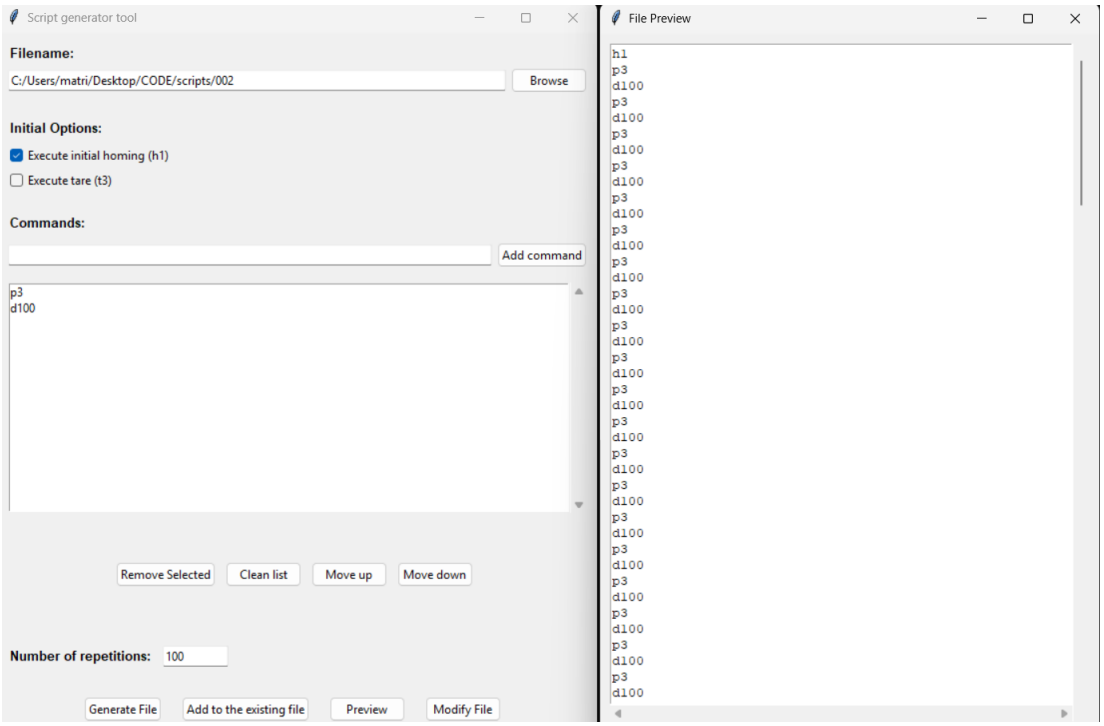

Figure 14 *The ScriptMaker GUI. The left panel allows for the selection of initial parameters (homing, tare) and the definition of command loops. The right panel provides a real-time text preview of the generated script file, ready for execution in LanGUImuir.*

Pseudocode

```
BEGIN Script_Generator

    // --- 1. Initialization Phase ---
    CREATE directory "scripts" if not exists
    INPUT Filename
    GET       Boolean       Flags:       Include_Homing,
Include_Calibration
    GET Integer: Loop_Iterations

    // --- 2. Content Construction ---
    INITIALIZE Command_Buffer as Empty List

    // Inject Setup Commands
    IF Include_Homing IS True:
        APPEND "h1" TO Command_Buffer
    IF Include_Calibration IS True:
        APPEND "t3" TO Command_Buffer

    // Inject User Sequence N times
    FOR i FROM 1 TO Loop_Iterations:
        FOR EACH Command IN User_Command_List:
            APPEND Command TO Command_Buffer
```

```
    // --- 3. File Output ---
    IF Mode IS "New File":
        WRITE Command_Buffer TO "scripts/Filename.txt"

    ELSE IF Mode IS "Append":
        // Intelligent Check
        IF   File   Exists   AND   (Include_Homing   OR
Include_Calibration):
            PROMPT User: "File exists. Do you really want
to re-initialize?"
            IF User_Declines:
                REMOVE     Setup     Commands     FROM
Command_Buffer

        APPEND Command_Buffer TO "scripts/Filename.txt"

    DISPLAY Success_Message

END
```

Full code available for implementation on GitHub, under MIT license, at:

https://github.com/DavideRmni/Scriptmaker

3.14 Future Expansions: Serial Connectivity and External Modules

The modular architecture of the Arduino-based system was designed to support future functional expansions beyond standard isotherm acquisition. A key feature of the chosen microcontroller (ATmega2560) is the availability of multiple serial communication ports (RX/TX) and digital I/O pins, which allow the system to interface with external peripherals.

Architecture for External Device Control

By leveraging the serial protocol, the central unit can send trigger signals or complex commands to auxiliary devices, synchronizing their operation with the barrier compression or expansion phases managed by LanGUImuir. This

capability transforms the trough into a versatile experimental hub, capable of coordinating multi-parametric assays. Potential integrations include:

- **Optical Sensors**: For real-time monitoring of subphase turbidity or fluorescence.
- **Laser Systems**: To perform surface-specific spectroscopy or interferometry.
- **Irradiation Modules**: For the study of light-responsive materials.

Implementation Example: In-situ UV Module As a proof of concept for this expandability, an in-situ UV irradiation module has been designed and partially implemented. The setup integrates a 365 nm UV LED equipped with a heatsink and a custom 3D-printed housing secured to a flexible, adjustable arm. Crucially, the LED driver is configured to receive control signals via the Arduino's serial port. This allows the software to trigger irradiation sequences automatically at specific surface pressures, demonstrating the system's ability to drive external hardware in a synchronized experimental workflow.

CHAPTER 4

GUV Electroformation Cells

4.1 Introduction

4.1.1 Background: GUVs as a model membrane system

Giant Unilamellar Vesicles (GUVs) represent a critical technology in biophysics and pharmaceutical sciences, serving as valuable model systems for investigating the topological and mechanical properties of biological bilayers [120, 121]. These structures play pivotal roles in diverse biotechnological applications, ranging from biochips and biosensors for medical diagnostics [122, 123] to advanced drug delivery vectors [124, 125]. The formation of GUVs relies on the amphipathic nature of lipids, which self-assemble to minimize the exposure of hydrophobic regions to water while maintaining hydration of their polar headgroups. This molecular organization is primarily driven by the hydrophobic effect [126, 127] and results in different lipid phases determined by chemical properties [128, 129], protein interactions [130, 131], and environmental factors such as temperature and phase composition.

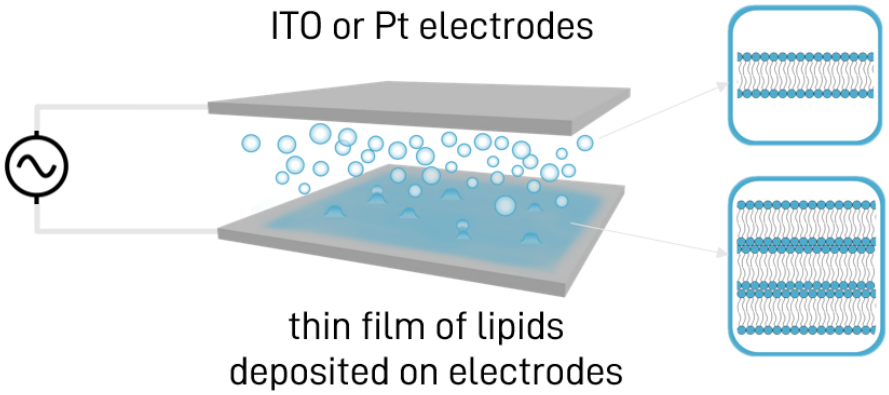

Figure 15 *Electroformation principle: AC field applies force on lipid layers to speed hydration and ease the formation of vesicles*

Among the various production methods, electroformation (Figure 15),originally developed by Angelova and Dimitrov [132, 133], remains the gold standard for generating defect-free GUVs. This technique involves the controlled hydration of lipid films deposited on conductive substrates under an

alternating current (AC) field. The resulting vesicle yield and morphology are strictly dependent on the lipid composition, peak-to-peak voltage (Vpp) frequency, and temperature [1, 134].

4.1.2 Limitations of standard ITO electrodes

Traditionally, the electroformation process employs Indium Tin Oxide (ITO) coated glass slides as electrodes. ITO is valued for its optical transparency, which facilitates real-time monitoring of vesicle growth [56, 133, 135, 136]. However, significant technical limitations hinder its widespread utility for large-scale or routine applications:

- **Fragility and Degradation:** ITO layers are mechanically fragile and prone to electrochemical degradation over time [137]. Repeated usage cycles lead to a progressive loss of conductivity and consistency in vesicle yield.
- **Maintenance:** While high-temperature annealing can partially restore electrode function, it does not fully regenerate the surface properties, leading to frequent replacement and increased operational costs.

4.1.1 The stainless steel alternative: Rationale

To overcome the limitations of ITO, selecting an appropriate electrode material is critical. While platinum wires and silicon substrates have been explored [138-141], austenitic stainless steel (304/316L) emerges as a superior candidate due to its unique physicochemical profile.

- **Chemical Stability:** The inherent passivation layer (Cr_2O_3) ensures high resistance in aqueous buffers, particularly at near-neutral pH, preventing electrode corrosion during electroformation.
- **Mechanical Robustness:** Unlike ITO, stainless steel tolerates rigorous handling, repeated cleaning cycles, and large-scale machining without performance loss.

- **Cost-Effectiveness:** It offers a scalable, economical alternative to noble metals or transparent conductive oxides.

In this study, we systematically investigate the use of stainless steel electrodes, specifically exploring novel mesh geometries, as a robust replacement for ITO. The primary objective is to optimize the electroformation setup by correlating electrode shape, AC frequency, and voltage with the yield and homogeneity of the GUV populations. By refining these physical parameters, we aim to establish a reproducible and scalable protocol for high-throughput membrane production.

4.2 Materials and methods

4.2.1 Reagents and Solutions

2-Oleoyl-1-palmitoyl-sn-glycero-3-phosphocholine (POPC), Sphingomyelin (SM), and Cholesterol (Chol) were purchased from Sigma-Aldrich (Milan, Italy) and used without further purification. Fluorescent probes Nile Red (NR) and Calcein, as well as D-glucose and sucrose for osmotic balancing, were also obtained from Sigma-Aldrich. All organic solvents utilized for lipid dissolution and cleaning (Chloroform, Methanol, Acetone, Isopropyl Alcohol) were of analytical grade. Austenitic stainless steel 304 mesh (400 grid) was sourced from Inoxia, while 316L stainless steel mesh (30 grid) was obtained as Nextmesh Coil SS from OFRF (Mingyou, China).

4.2.2 Fabrication of electroformation chambers

Four distinct electrode configurations were designed and fabricated to evaluate the impact of geometry on vesicle yield. The fabrication approach varied by design: while Chambers A and D utilized standard mechanical assembly, Chambers B and C required custom additive manufacturing to achieve complex geometries.

3D Printing and Assembly (Chambers B & C)

Small structural components for Chambers B and C were fabricated using an Elegoo Mars SLA printer (Guangdong, China) with proprietary photopolymer resin. Post-printing, components were bonded using Weicon VA8312 cyanoacrylate adhesive and treated with sodium carbonate to enhance chemical resistance against organic solvents.

- **Chamber B**: Designed as a coaxial system, it featured a central hypodermic needle housed within a 304 stainless steel mesh cylinder (⌀ ≈ 3.2 mm). A custom 3D-printed housing was engineered to maintain the concentric alignment of the electrodes.
- **Chamber C**: Consisted of two parallel 3D-printed frames (7.7 × 42mm) holding fine stainless steel mesh (400 grid) at a fixed distance of 1.6 mm. The printed frames were essential to maintain uniform spacing and tension of the fine mesh.

Standard Mechanical Assembly (Chambers A & D)

- **Chamber A**: Followed the classic design by Pereno et al. [139], utilizing two 21G hypodermic needles (0.8 × 38 mm) arranged in parallel through a standard glass vial cap with a spacing of 1.6 mm.
- **Chamber D**: Featured broad strips of 316L stainless steel mesh (30 grid) spaced at 1.4 mm. In this configuration, hypodermic needles served solely as structural supports for the mesh, without acting as primary electrodes.

Prior to every use, all stainless steel components were rigorously cleaned with isopropyl alcohol, distilled water, and acetone to remove surface contaminants.

4.2.3 Electronic setup and electroformation protocol

An **FG-100 DDS** function generator (SC Electronic, Guangdong, China) was employed to generate the AC field (sinusoidal and square waves). The low-power USB-driven device ensured minimal thermal drift. The temperature was strictly controlled using a thermostatic bath. The electroformation protocol involved the deposition of the lipid solution (1.0 mg/mL or 0.4 mg/mL) onto the electrode surface until saturation. After vacuum drying to remove solvent traces, the chamber was filled with a 0.2 M sucrose solution. The electrical stimulation followed a multi-step ramp-up sequence to minimize bilayer stress, typically transitioning from a sinusoidal wave for vesicle growth to a square wave for detachment.

4.2.4 Microscopy and data acquisition

Harvested vesicles were resuspended in an iso-osmolar 0.2 M glucose solution to facilitate sedimentation. Imaging was performed using two systems:

- **Fluorescence Microscopy:** An Axioplan 2 (Carl Zeiss) with a Plan Neofluar 40×/1.30 oil immersion objective.
- **Confocal Microscopy:** A Leica TCS MP5 laser scanning microscope with a 20×/0.55 dry objective (488 nm excitation). Fluorescence emission was collected in the 500–530 nm range for Calcein and 569–650 nm for Nile Red.

4.2.5 Computational image analysis

To ensure unbiased sizing and counting, equatorial diameters were computed using a custom semi-automated workflow developed in Python 3.12. The pipeline utilized OpenCV (Canny edge detection, HoughCircles) and scikit-image to identify vesicles in z-stacks. The algorithm automatically selected the equatorial slice by maximizing the radius subject to circularity (>0.90) and edge signal-to-noise ratio constraints.

4.2.6 Yield quantification

To provide a robust metric for electroformation efficiency, the lipid incorporation yield (η) was calculated following the geometric approach described by Cooper et al. [142], the yield is defined as as the ratio between the moles of lipid incorporated into vesicles (n_{mem}) and the total moles of lipid initially dosed on the electrode (n_{dosed}).

The total lipid dose was converted into an equivalent bilayer area (A_{dep}) and expressed in moles using the area per lipid headgroup (a_0):

$$n_{dosed} = \frac{A_{dep}}{a_0 N_A}$$

Equation 6 *Calculation of total lipid moles deposited on the electrode*

Where A_{dep} represents the theoretical membrane area corresponding to the applied lipid dose (calculated from the deposited volume and concentration), a_0 is the molecular area per lipid (approximated as 0.65 nm^2 for POPC), and N_A is Avogadro's number.

Similarly, the lipid incorporated into vesicles was quantified by summing the surface areas of all detected GUVs. To focus on biologically relevant GUVs, only vesicles with a diameter >10µm were included in the yield metric, while smaller vesicles were excluded. Assuming **unilamellarity** for all selected vesicles, the membrane area for each vesicle *i* was calculated as $Ai = 8\pi r2$ (accounting for the two leaflets of the bilayer).

$$n_{mem} = \frac{A_{mem}}{a_0 N_A}$$

Equation 7 *Quantification of lipid moles incorporated into vesicle membranes*

Here A_{mem} is the total bilayer area obtained from the fluorescence images. For each vesicle *i*, the membrane area was calculated as the total area A_{mem} was then derived by scaling the sum of vesicle areas by the field-of-view factor (*S*).

To ensure quantitative reliability while managing computational load, vesicle counting was performed using a **convergence-based sampling strategy**. The total membrane area was computed from a progressively expanding set of non-overlapping fields of view until the yield estimate converged to a stable value. While the absolute number of counted vesicles (N ≈ 640) is lower than large-scale automated studies [142-144] , this approach ensures statistical sufficiency for the comparative analysis of chamber geometries.

4.2.7 Automated lipid stoichiometry and preparation

To ensure high reproducibility in membrane composition and minimize pipetting errors during the preparation of complex ternary mixtures, a custom Python utility was developed. The software automates the stoichiometric calculations required to translate desired molar ratios into precise volumetric aliquots from lipid stock solutions.

Database and Parameter Management

The application is built upon a dynamic JSON database that stores the physicochemical properties of lipids and fluorescent probes. For each compound, the system records:

- Molecular Weight (MW): Essential for molar-to-mass conversion.
- Phase Transition Temperature (T_m): Displayed to assist the user in selecting an appropriate electroformation temperature ($T>T_m$) to ensure the bilayer remains in the fluid phase.The interface is organized into two functional modules (Figure 16a, 16b): a Calculation Tab for defining experimental parameters and a Database Tab for managing the library of compounds.

Calculation Algorithm

The user inputs the target final concentration (C_{Target}), the total volume of the lipid mixture (V_{Tot}), and the desired molar percentages for up to six lipid components plus a fluorescent probe. The script executes the following logic to compute the required aliquots.

Pseudocode

```
BEGIN Lipid_Calculator

    // --- Initialization ---
    LOAD Database (Lipids, Probes) from JSON
    INPUT Target_Concentration (mM)
    INPUT Total_Volume (mL)
    INPUT     List     of     Selected_Lipids     (Name,
Molar_Percentage, Stock_Concentration_mg_mL)
    INPUT   Probe_Settings   (Name,   Probe_Percentage,
Stock_Mode, Stock_Value)

    // --- Main Calculation ---
    // 1. Calculate Total Moles required in the final
vial
    Total_Moles = Target_Concentration * Total_Volume

    // 2. Lipid Aliquots Calculation
    FOR EACH Lipid IN Selected_Lipids:
        // Moles required for this specific lipid
        Moles_Lipid = Total_Moles * (Lipid.Percentage /
100)

        // Convert to Mass (mg)
        MW = Database.GET_MW(Lipid.Name)
        Mass_Lipid_mg = Moles_Lipid * MW

        //  Calculate  Volume  to  pipette  from  stock
solution (microliters)
        // V = (Mass / Concentration) * 1000
        Volume_uL       =       (Mass_Lipid_mg       /
Lipid.Stock_Concentration_mg_mL) * 1000

        DISPLAY Volume_uL for Lipid

    // 3. Probe Calculation (Added on top of lipids)
    Probe_MW = Database.GET_MW(Probe.Name)
    Moles_Probe = Total_Moles * (Probe.Percentage / 100)
```

```
    IF Probe.Stock_Mode IS "Molar":
        // If stock is defined in mM
        Stock_Molar = Probe.Stock_Value
        Probe_Volume_uL = (Moles_Probe / Stock_Molar) *
10^6

    ELSE IF Probe.Stock_Mode IS "mg/mL":
        // If stock is defined in mass/volume
        Stock_mg_mL = Probe.Stock_Value
        Probe_Volume_uL = ((Moles_Probe * Probe_MW) /
Stock_mg_mL) * 1000

    DISPLAY Probe_Volume_uL

    // --- Data Export ---
    SAVE parameters and results to CSV/JSON for
experiment logging

END
```

The source code implementing this algorithm is released under the MIT License. https://github.com/DavideRmni/Lipid_calculator

This automated workflow eliminates manual calculation errors and ensures that the final lipid film deposited on the electrodes possesses the exact stoichiometry required for the experiment, regardless of the differing molecular weights of the components.

a) b)

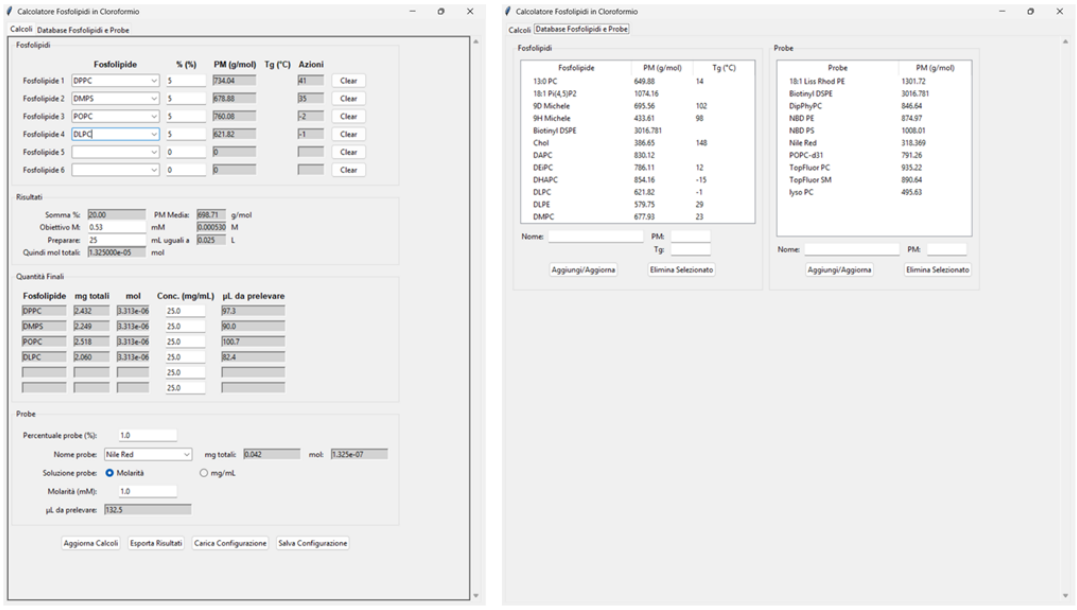

Figure 16 *Graphical User Interface of the Lipid Calculator. (a) The main calculation panel allows the user to define the target concentration, select lipids from the database, and input stock concentrations. The system automatically computes the volume (µL) to be pipetted. (b) The database management tab allows for the addition and modification of lipid parameters (Molecular Weight, T_m) and fluorescent probes.*

4.3 Results and discussion

4.3.1 Electroformation chamber design optimization

The study systematically evaluated four distinct chamber configurations to optimize the physical parameters governing electroformation on stainless steel substrates. To visualize the geometric differences, the 3D designs and actual photographs of the fabricated chambers are presented in Figure 17.

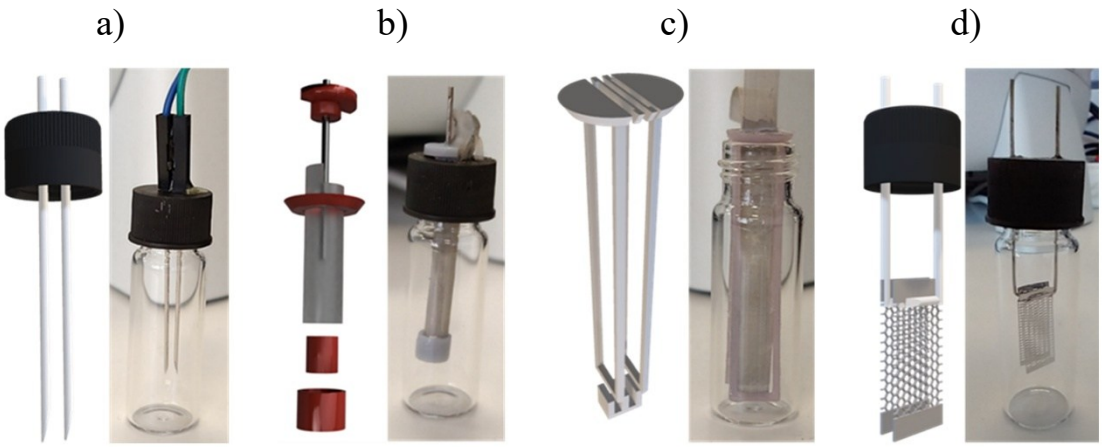

Figure 17 *The four different electroformation chambers. For each panel, 3D design representations of the electrodes are displayed on the left, and a photograph of the actual chamber is shown on the right. (a) Chamber A; (b) Chamber B; (c) Chamber C; (d) Chamber D*

Performance Analysis of Chamber Configurations

- **Chamber A (Parallel Needle Configuration):** This initial design closely resembles the system described by Pereno et al. [139], with two 21G hypodermic needles arranged in parallel at a distance of 1.6 mm. While it achieved a moderate vesicle yield with a relatively uniform size distribution, the limited surface area of the needles restricted the total lipid loading capacity.
- **Chamber B (Coaxial Needle-Mesh):** Designed to increase surface area using a cylindrical mesh counter-electrode. However, practical implementation revealed severe operational constraints: the coaxial geometry made the homogenous deposition of the lipid film extremely difficult, resulting in uneven coating and poor reproducibility. Consequently, this configuration was discarded.
- **Chamber C (Frame-Supported Fine Mesh):** This design utilized fine 400-mesh grids supported by 3D-printed frames to maximize capillary retention. Despite favorable deposition properties, experimental trials consistently resulted in **negligible vesicle yield** ("No vesicles"). We suggest this may be due to an **unfavorable electric field distribution**:

the fine grid likely retained the lipid solution deeply within its interstices, where the field strength was insufficient to drive bilayer swelling and vesicle detachment.

- **Chamber D (Wide Mesh on Needle Support):** This configuration featured a broader stainless steel mesh (Mesh 30) supported by structural needles. The mesh provided a significantly larger surface area (~0.8mL deposition capacity) compared to needle-only designs. The open geometry ensured a homogenous electric field distribution, reducing localized distortions. As a result, Chamber D consistently produced the highest GUV yield with superior morphological quality and was selected as the optimal design for further parametric studies.

4.3.2 Optimization of electroformation parameters

The efficiency of the electroformation process is governed by a complex interplay of parameters, including the amplitude of the alternating current, frequency, electrode spacing, and lipid layer thickness [1, 145]. To identify the optimal protocol for the stainless steel setup, a systematic screening was conducted by varying the peak-to-peak voltage (Vpp) and frequency (Hz). The outcomes of these trials are detailed in Table 2

	Chamber A	**Chamber B**	**Chamber C**	**Chamber D**
Resistance (MΩ) with POPC 1.32 mM	4.9 ± 0.1	1.5 ± 0.1	5.3 ± 0.1	4.7 ± 0.1
0.0V_{pp}, 0.0 Hz, 38°C, POPC 1.32 mM	No vesicles	No vesicles	No vesicles	No vesicles
5.0 V_{pp}, 800 Hz, 38°C, POPC 1.32 mM	Vesicle formation Multivesicular Irregular shape	Irregular formations	No vesicles	Vesicle formation Multivesicular
4.4 V_{pp}, 500 Hz, 38°C, POPC 1.32 mM	Vesicle formation Irregular shape	Vesicle in a vesicle formation low yield	No vesicles	Vesicle formation Irregular shape

4.0 V_{pp}, 100 Hz, 38°C, POPC 1.32 mM	Irregular shape	Irregular formations low yield	No vesicles	Vesicles Multivesicular Irregular shape
4.8 V_{pp}, 200 Hz, 38°C, POPC 1.32 mM	Irregular shape	Irregular formations low yield	No vesicles	Vesicle formation Irregular shape
4.8 V_{pp}, 400 Hz, 38°C, POPC 1.32 mM	Small vesicles Irregular shape	Small vesicles low yield	No vesicles	Small vesicles Multivesicular
5.0 V_{pp} 400 Hz 38°C, POPC 1.32 mM	Small vesicles Irregular shape	Small vesicles low yield	No vesicles	Small vesicles Multivesicular
4.8 V_{pp} 800 Hz, 38°C, POPC 1.32mM	Irregular shape	Multivesicular low yield	No vesicles	Vesicles, Irregular shape, Vesicle in a vesicle
4.4 V_{pp}, 500 Hz, 38°C, POPC 0.5 mM	Vesicle formation			Vesicle formation
4.4 V_{pp}, 200 Hz, 70°C, POPC:SM:Chol (2:1:1) 0.5 mM	Vesicle formation Irregular shape			Vesicle formation Irregular shape
4.4 V_{pp}, 400 Hz, 70°C POPC:SM:Chol (2:1:1) 0.5 mM	Vesicle formation			Vesicle formation

Table 2 Screening of electroformation parameters. Observations refer to vesicles formed on stainless steel electrodes (Chamber D) unless otherwise noted.

Frequency Tuning

The screening confirmed that optimal frequencies lie below 10 kHz. This aligns with established theory, as these frequencies correspond to timescales shorter than the inverse of Maxwell-Wagner-Sillars polarization in the membrane [146]. Frequencies significantly higher than this threshold fail to produce significant perturbations in the phospholipid bilayer, hindering vesicle swelling.

Voltage Optimization

Regarding voltage, a critical window was identified between **4.0 and 4.5 V**. This range is dictated by the dielectric constant of the heterogeneous system and the interelectrode distance.

- Dielectric Breakdown: If the voltage exceeds the threshold of 5.0 V, unrestricted current flows between the electrodes. This phenomenon disrupts the electroformation process, leading to hydrolysis or thermal damage, often resulting in the formation of multilamellar vesicles (MLVs) or irregular structures (Figure 18).
- Lipid Loading Effect: It was observed that high phospholipid loading increases the effective dielectric constant, providing greater tolerance to higher voltages, though at the cost of increased defect formation.

Based on these findings, the optimized protocol established 4.4 Vpp at 500 Hz as the standard condition for high-quality GUV production across most lipid mixtures.

4.3.3 Impact of lipid concentration and defect minimization

High lipid loading frequently resulted in the formation of aberrant structures, such as multilamellar vesicles (MLVs) and multivesicular bodies (Figure 18). To suppress MLV formation and promote unilamellarity, the lipid stock concentration was reduced to 0.53 mM (approx. 0.4 mg/mL). This dilution ensured complete saturation of the electrode surface with a consistent phospholipid monolayer rather than multilayers. The optimized deposition volume was found to be ~400 µL for Chamber D.

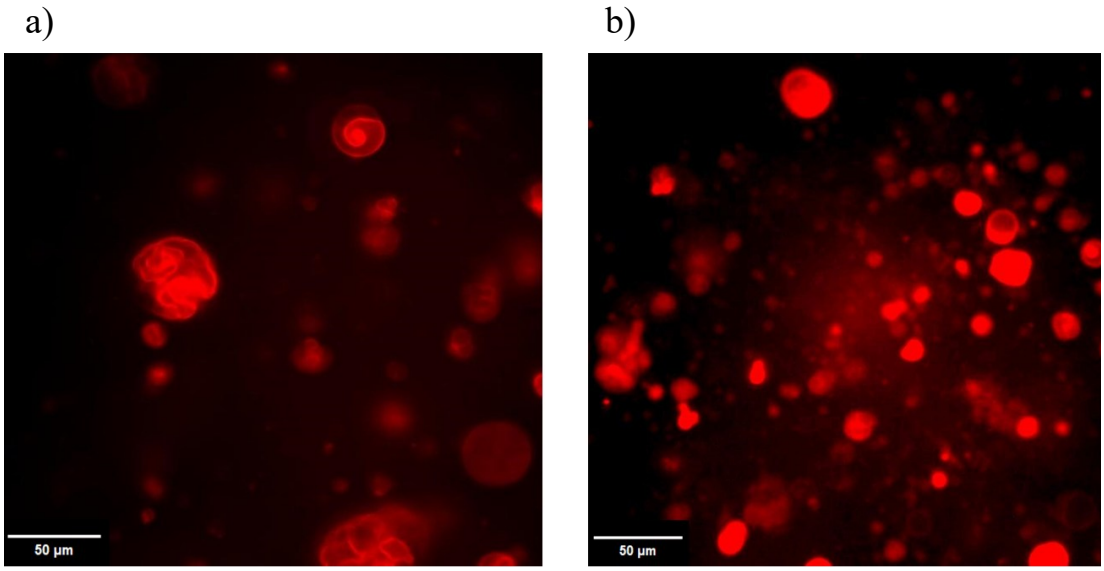

Figure 18 *Defects arising from non-optimal conditions (excess lipid loading). (a) Irregular formations obtained at 4.8 Vpp, 200 Hz. (b) Multilamellar POPC formations obtained at 5.0 Vpp, 800 Hz.*

4.3.4 Refined electroformation protocols

Based on the parametric screening, two distinct protocols were established:

- **Standard Protocol (POPC):** Temperature at 37.0°C. Constant voltage at 4.4 Vpp (500 Hz, sine wave) for 60 min, followed by detachment at 2.2 Vpp (250 Hz, square wave).
- **Complex Ternary Mixture (POPC:SM:Chol 2:1:1):** To handle high-transition temperature lipids, the bath temperature was increased to 70°C. The voltage was ramped gradually to 4.0 Vpp, with a frequency of 400 Hz (sine wave) for formation, followed by 200 Hz (square wave) for detachment.

4.3.5 Encapsulation verification

To confirm that the structures formed were indeed hollow GUVs, electroformation was conducted in a solution containing calcein (fluid-phase marker) and sucrose. As shown in Figure 19, the resulting vesicles exhibited a clear green fluorescence in the internal lumen (calcein) and red fluorescence on

the membrane (Nile Red). The successful encapsulation confirms the structural integrity and unilamellarity of the vesicles produced by the stainless steel mesh.

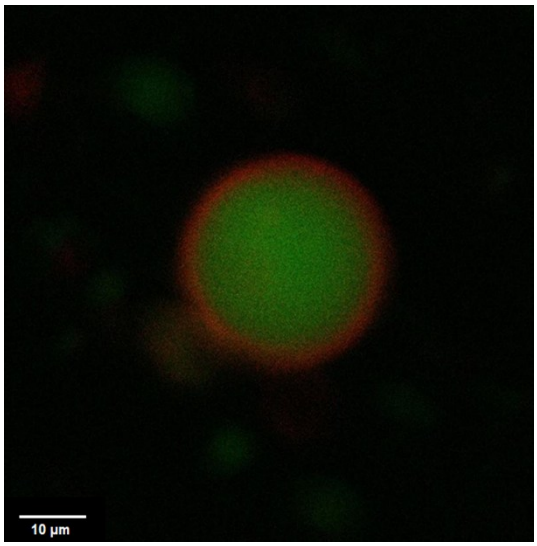

Figure 19 *Isolated GUV filled with calcein, Nile Red used as membrane probe*

4.3.6 Quantification of vesicle yield

The quantification of lipid incorporation (η) was performed on the optimized Chamber D configuration, restricting the analysis to GUVs with diameters ≥ 10µm. Based on the deposition of 400 µL of a 0.53 mM POPC solution, the total lipid load was calculated as approximately 2.12×10^{-7} mol.

As summarized in Table 3, the counting statistics over 4 independent replicates yielded a mean density of 160 ± 22 vesicles per field, resulting in an incorporation yield of 0.20 ± 0.03%.

While this absolute value is lower than theoretical maximums, it accurately reflects the mechanics of electroformation on metal substrates: the proximal lipid bilayer adheres strongly to the electrode surface and typically does not participate in the budding process [1]. However, unlike standard ITO protocols where delamination can be erratic, the stainless steel mesh demonstrated a highly reproducible detachment efficiency, confirming its suitability for consistent biophysical assays.

Metric	Symbol	Value (mean ± SD)	95% confidence interval	Total vesicles > 10 µm	Fields and replicates
Vesicle count per field	N_{field}	160 ± 22	[149, 171]	640	4
Mean vesicle diameter	d_{mean}	17.3 ± 4.1 µm	[15.0, 19.6]	–	4
Lipid moles in GUV > 10 µm	n_{GUV}	(4.17 ± 0.52) × 10^{-10} mol	[3.70, 4.64] × 10^{-10}	–	4
Total lipid added	n_{loaded}	6.36 × 10^{-7} mol	–	–	–
Yield (% of lipid in GUV > 10 µm)	**η**	**0.20 ± 0.03 %**	**0.22 %**	–	4

Table 3 Quantification of POPC GUV yield (Chamber D)

4.3.7 Size and distribution analysis

To further validate the superiority of the mesh design, the size distribution of the GUV populations was analyzed. As illustrated in Graph 4, there is a marked difference in the population profiles:

- Chamber A (Needles): Produced a narrower distribution with a lower count of large vesicles.
- Chamber D (Mesh 30): Exhibited a broader distribution (Graph 4) with a significantly higher frequency of GUVs in the 20–50 µm range.This shift towards larger diameters confirms that the uniform field and larger surface area of the mesh electrode not only increase the total yield (as shown in Table 3) but also promote the growth of larger, defect-free vesicles.

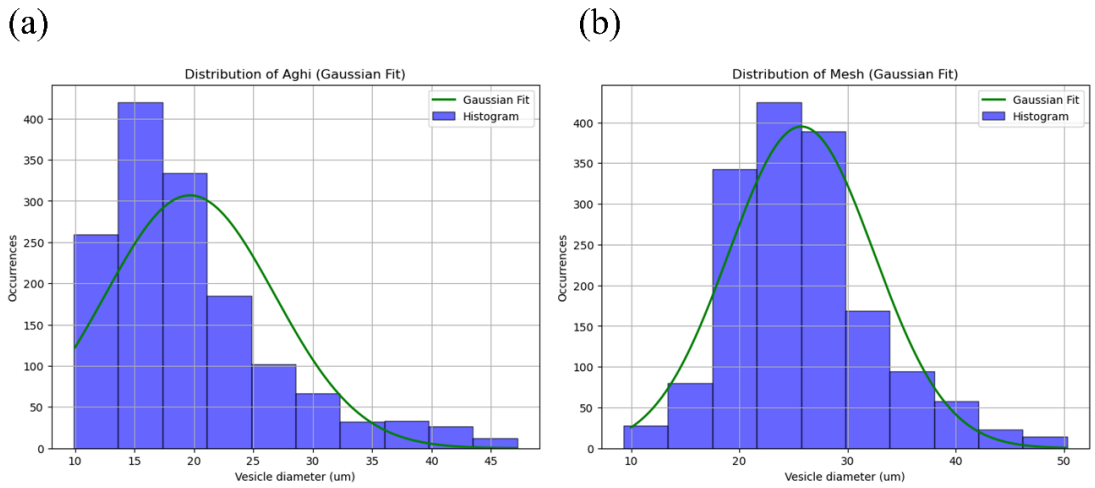

Graph 4 *Size distribution histograms of POPC vesicles (>10 µm). (a) Vesicles produced using steel needles in Chamber A. (b) Vesicles generated with the steel mesh apparatus in Chamber D. The mesh configuration yields a significantly higher count of large GUV*

4.3.8 Effect on lipid composition

The formation of vesicles from a ternary mixture (POPC:SM:Chol 2:1:1) was compared to pure POPC. While POPC vesicles displayed high homogeneity, the ternary mixture yielded vesicles with enhanced structural integrity due to the rigidifying effect of cholesterol and sphingomyelin. As shown in Figure 20, the ternary mixture showed varied fluorescence intensity, reflecting the heterogeneous distribution of lipids, consistent with the expected phase behavior of complex membranes.

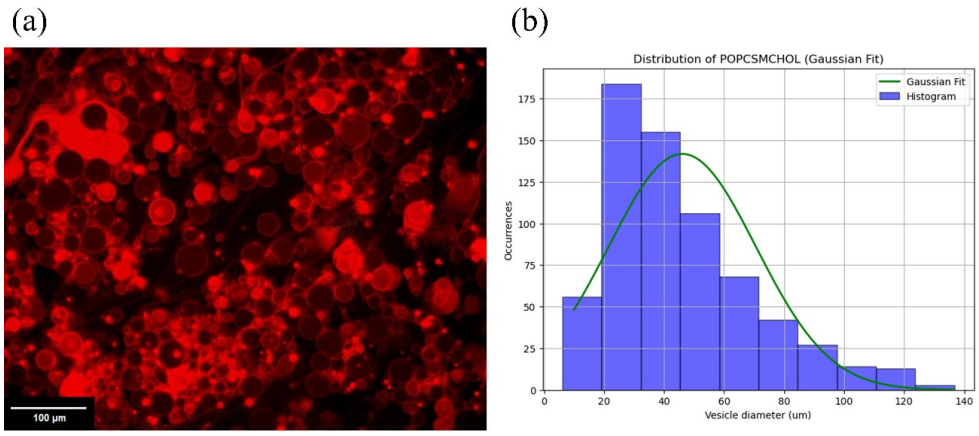

Figure 20 *Vesicles of POPC:SM:Chol (2:1:1) obtained from Chamber D. (a) Fluorescence microscopy showing intensity variations. (b) Size distribution histogram indicating a more heterogeneous population compared to pure POPC.*

4.4 Applications in Membrane Biophysics

To demonstrate the versatility of the developed electroformation setup beyond standard characterization, the device was employed to investigate the biophysical properties of membranes under varying environmental and compositional conditions. These studies were conducted in collaboration with the Laboratory of Prof. Granjon and Prof. Maniti (University of Lyon, Lyon, France).

4.4.1 Investigation of membrane fluidity and rigidity

Membrane fluidity was assessed using DiOll, a fluorescent probe derived from Laurdan, which is sensitive to the hydration and packing order of the lipid bilayer. The spectral shift of DiOll emission allows for the calculation of the Generalized Polarization (GP) parameter, defined as:

$$GP = \frac{(I_{440} - I_{490})}{(I_{440} + I_{490})}$$

Equation 8 *Equation of the General Polarization used for measuring membrane elasticity*

Where I_{440} and I_{490} correspond to the fluorescence intensities at the emission maxima for the gel (ordered) and liquid-crystalline (fluid) phases, respectively. High GP values indicate a rigid, ordered membrane, while low GP values suggest a fluid, disordered state (Graph 5).

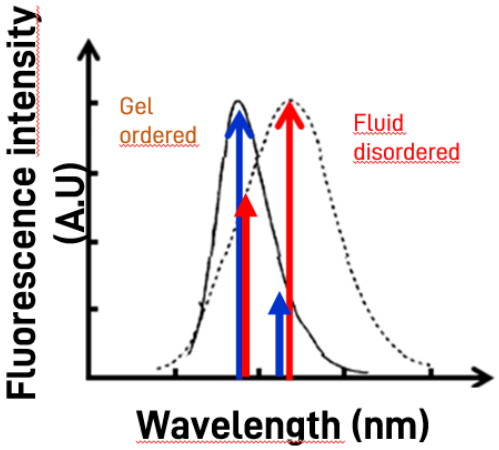

Graph 5 *Principle of membrane fluidity measurement using the DiOll probe. The emission spectrum shifts from blue (440 nm, ordered) to red (490 nm, fluid) depending on the lipid packing density. Adapted from Parasassi et al..*

Impact of Environmental and Structural Factors

Using GUVs produced with the stainless steel mesh setup (Chamber D), correlations were established between membrane rigidity and three key variables: aqueous environment, vesicle size, and lipid composition.

- **Buffer Composition**: The nature of the hydration solution significantly influenced membrane packing. Vesicles electroformed and maintained in sucrose/glucose solutions exhibited the highest rigidity compared to those in MilliQ water or HEPES/NaCl buffers. This suggests that sugar molecules may interact with the lipid headgroups or modify the water structure at the interface, stabilizing the bilayer (Graph 6a).
- **Vesicle Size (Curvature Stress)**: A comparison between Giant Unilamellar Vesicles (GUVs) and Large Unilamellar Vesicles (LUVs) obtained by freeze-thawing and extrusion, revealed that GUVs generally

display higher fluidity. Interestingly, among the sub-micron populations, 400 nm LUVs appeared to be the most rigid formations. This highlights the role of membrane curvature in lipid packing density (Graph 6b).

- **Lipid Composition and Cholesterol**: The addition of cholesterol to POPC membranes showed a concentration-dependent effect. Consistent with literature, low concentrations of cholesterol tended to enhance fluidity by disrupting the tight packing of phospholipids, whereas higher concentrations promoted rigidity (ordering effect), increasing the GP value (Graph 6c).

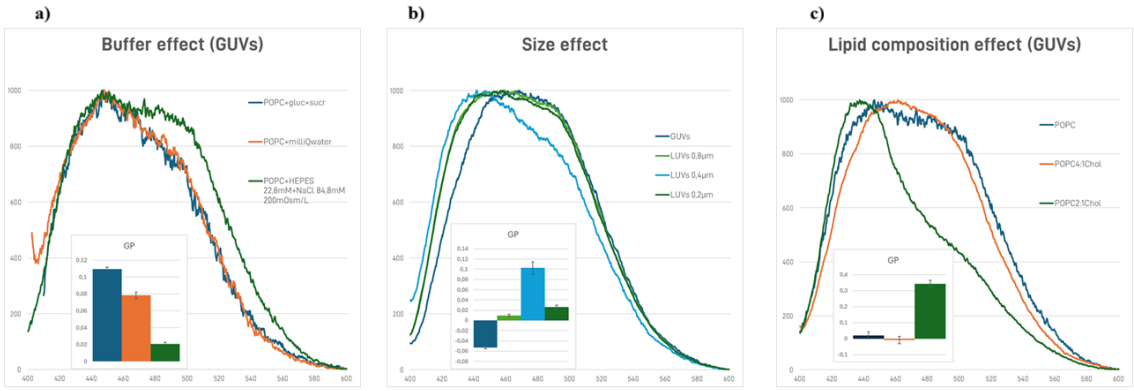

Graph 6 *Gp comparison between different conditions: a) buffer composition, b) size of liposomes, in comparison with LUVs made by freeze thawing and extrusion, and c) lipid composition*

Temporal Stability and Size Control

To evaluate the aging of the model system, stability tests were performed on POPC:Chol (4:1) vesicles over a 72-hour period. A comparison of the emission spectra acquired on day 1 and day 3 revealed a significant shift in the spectral profile and the resulting Generalized Polarization (GP) value (Graph 7).

This spectroscopic variation, coupled with microscopic observations of vesicle rupture over time, indicates that the structural integrity of this specific lipid formulation is time-dependent. These findings underscore the necessity of performing biophysical assays on freshly prepared samples to ensure data reliability.

Conversely, regarding the control of vesicle morphology during fabrication, a positive correlation was established between the deposited lipid amount and the final dimensions. As shown in Table 4 varying the deposition volume from 150 to 400 µL resulted in a modulation of the vesicle diameter, allowing for coarse tuning of the GUV population size to suit specific experimental needs.

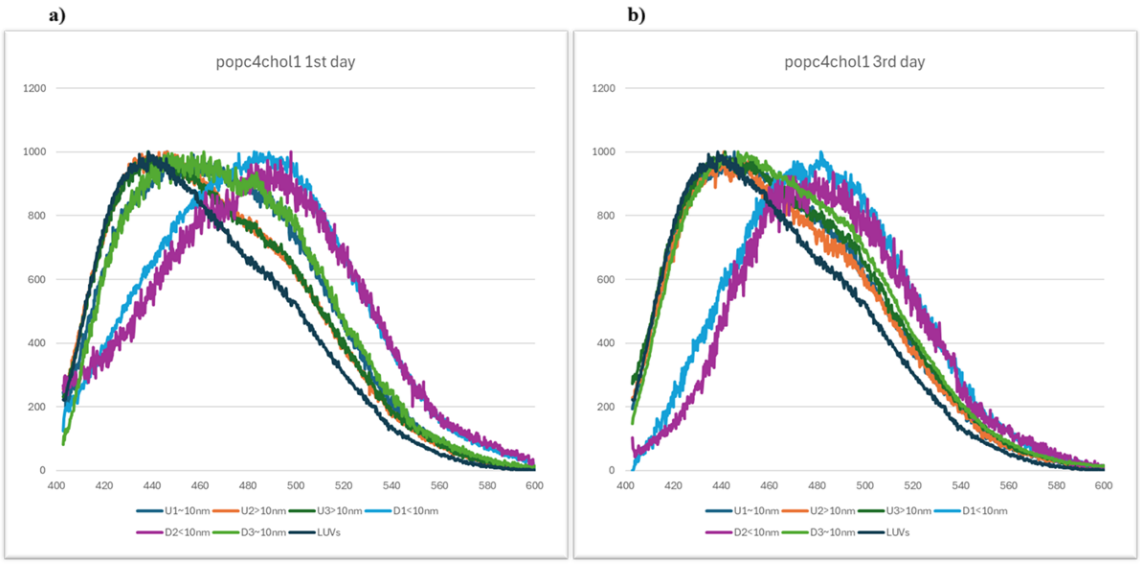

Graph 7 *Stability of POPC:Chol (4:1) vesicles over time. The observed spectral shift indicates a modification of the membrane properties over time, associated with vesicle instability.*

	150 µL	300 µL	400 µL
U – Upper solution	~10µm	>10µm	>10µm
D – Lower solution	<10µm	<10µm	~10µm

Table 4 *Correlation between the volume of deposited lipid solution (0.5 mM) and the observed vesicle diameter. Larger deposition volumes tend to favor the formation of larger GUVs (>10 µm).*

4.4.2 Stress with complex mixtures: DPPC:DPPS:DLPC

To evaluate the limits of the electroformation setup with high-melting-point and charged lipids, a ternary mixture of DPPC:DPPS:DLPC (6:2:2) was tested. This formulation presents significant challenges due to the high phase transition

temperature (Tg) of DPPC (41°C) and DPPS (54°C), requiring elevated working temperatures.

Experimental trials revealed significant issues regarding **processability and thermolability**. While vesicle formation was initially observed at high temperatures, the system demonstrated extreme instability during the harvesting phase. As illustrated in Figure 21, the degradation process was rapid:

- Post-Formation: Immediately after collection from the cell (maintained at ~60°C), vesicles were visible and ostensibly intact.
- Cooling Phase: As the sample temperature approached room temperature, marked morphological irregularities and deformations appeared.
- Collapse: Upon reaching thermal equilibrium at room temperature, the vesicular structures completely disintegrated, leaving only amorphous lipid precipitates.

This finding identifies a specific operational boundary for the current setup when handling highly thermolabile complex mixtures that require strict temperature control not only during formation but also during observation.

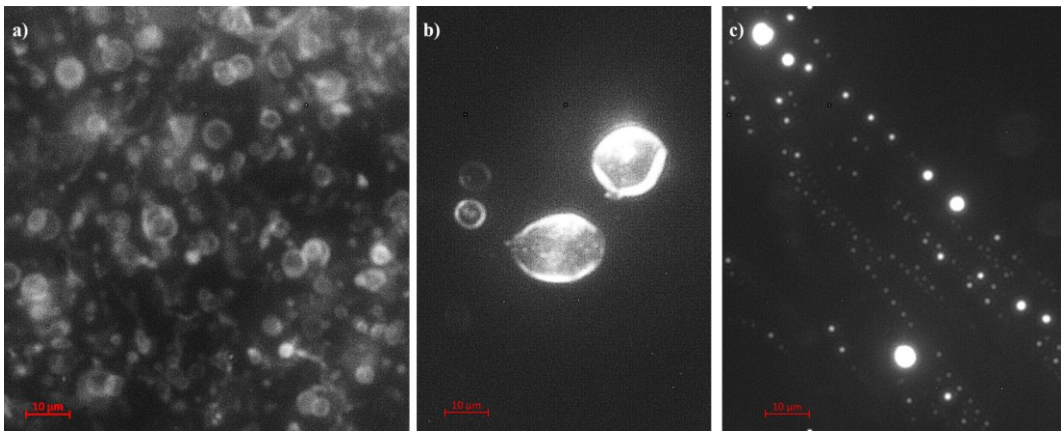

Figure 21 *Stability assessment of DPPC:DPPS:DLPC (6:2:2) vesicles. (a) Sample aliquot immediately collected from the electroformation cell. (b) Isolated vesicles observed during cooling to room temperature, exhibiting morphological irregularities. (c) Final state at room temperature, showing complete vesicle disruption and lipid precipitation.*

4.4.3 Application in translocation studies

Finally, the electroformation setup was employed to investigate the internalization mechanism of Cell-Penetrating Peptides (CPP). Since electroformed vesicles are biomimetic systems devoid of metabolic activity and endocytic machinery, they serve as an ideal negative control to distinguish between active uptake (endocytosis) and direct physical permeation (translocation).

Protocol Adaptation: Intentional MLV Generation While the primary goal of the thesis was the production of unilamellar vesicles (GUVs), for this specific assay, Multi-Lamellar Vesicles (MLVs) and multi-vesicular structures were preferred. In standard GUVs, discriminating between a peptide bound to the outer surface and one truly dissolved in the internal lumen can be optically challenging due to the limited z-resolution of fluorescence microscopy. Conversely, MLVs—characterized by concentric bilayers or "vesicles-within-vesicles"—offer multiple internal aqueous compartments. Detecting fluorescence within an inner vesicle provides unambiguous proof that the peptide has crossed the outer barrier. To achieve this, the electroformation parameters were intentionally modified (e.g., by increasing lipid loading or voltage stress) to favor the formation of complex multi-layered structures. This adjustment highlights the versatility of the control system, which allows the user to fine-tune the outcome from pure GUVs to MLVs depending on the analytical requirement.

Experimental Verification Fluorescently labeled CPPs were incubated with the MLV suspension. Fluorescence microscopy revealed the accumulation of the peptide not just on the outer membrane, but within the internal vesicles (Figure 22). Given the artificial nature of the system, this observation provides clear evidence that the peptide is capable of crossing lipid bilayers via passive translocation, independent of cellular pathways.

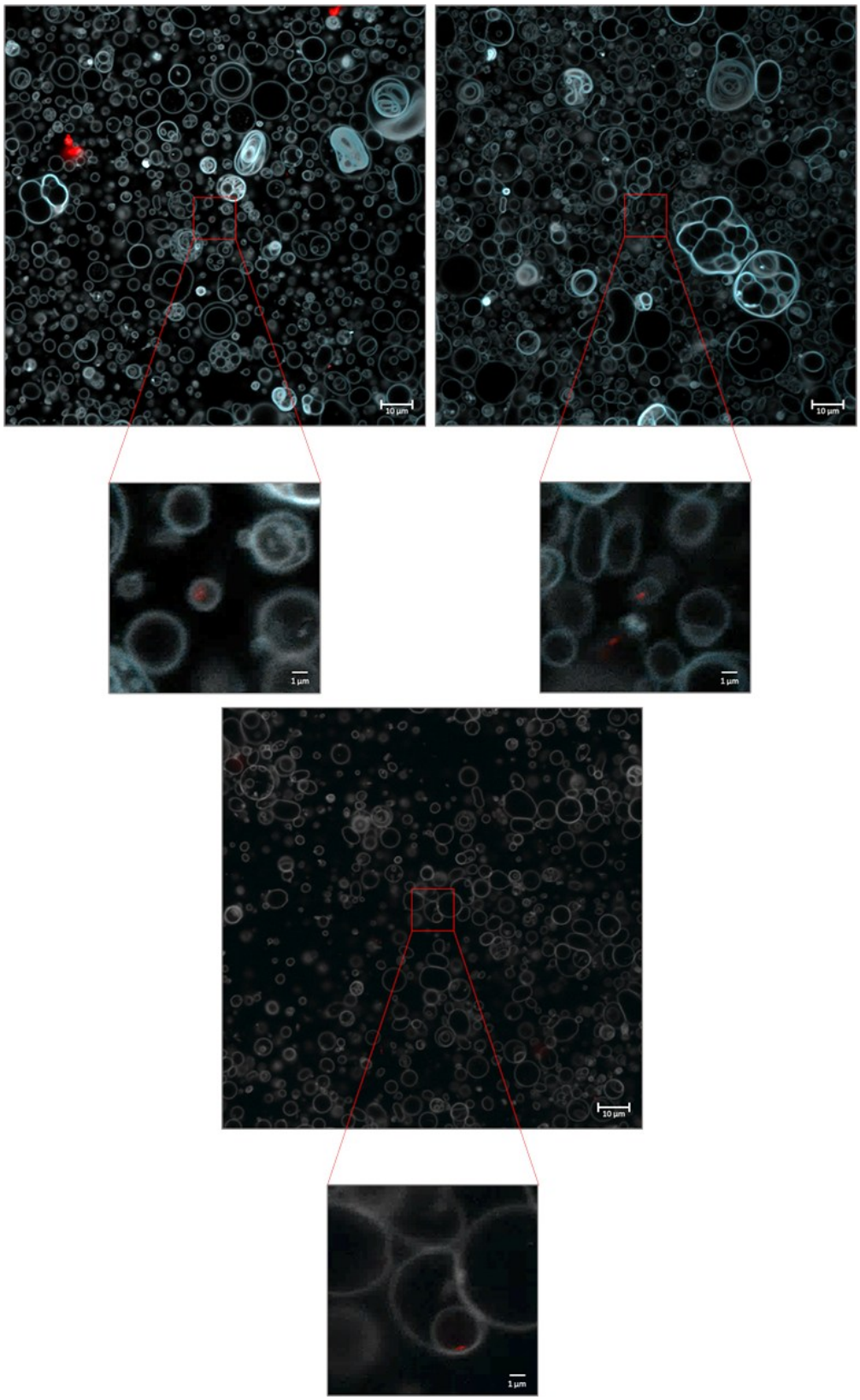

Figure 22 *Translocation assay of Cell-Penetrating Peptides (CPP) in Multi-Lamellar Vesicles (MLVs). The presence of fluorescence inside the internal "daughter" vesicles confirms that the peptide successfully crossed the outer lipid barriers via direct translocation.*

4.5 Conclusions

This study demonstrates that stainless steel electrodes are a practical and effective alternative to conventional indium tin oxide electrodes for the electroformation of giant unilamellar vesicles. Compared with ITO, stainless steel offers greater durability, lower cost, and wider availability, making it well-suited for large-scale vesicle production.

Systematic evaluation of electrode shapes and configurations revealed that geometry, applied voltage, and frequency significantly affect vesicle yield and quality. Among the designs tested, the broad 316L stainless steel mesh-30 electrodes (Chamber D) produced the highest yields, with a greater proportion of single vesicles and reduced size heterogeneity. Under optimized electrical parameters (4.4 Vpp, 500 Hz), the setup achieved a reproducible lipid incorporation yield of 0.20%. Although this absolute value is lower than theoretical maximums due to the strong adhesion of the proximal lipid bilayer to the metal surface, it ensures a detachment efficiency sufficient for high-throughput biophysical assays.

Importantly, the Chamber D design simplifies phospholipid deposition and demonstrates versatility: it allows for the production of both standard GUVs and, through protocol adaptation, Multi-Lamellar Vesicles (MLVs) for specific translocation assays. By integrating common, low-cost stainless steel materials with automated protocol management, we demonstrate a scalable approach for producing high-quality GUVs suitable for biophysical studies of membrane dynamics and drug delivery applications.

CHAPTER 5

Computational Tools for Data Analysis and Automation

5.1 Introduction

The experimental work described in this thesis generates vast datasets, particularly in the context of fluorescence spectroscopy applied to membrane biophysics. A significant portion of the data analysis framework was developed during a research period at the Laboratory of Prof. Granjon and Prof. Maniti (France). Their research focuses heavily on assessing membrane flexibility using novel Laurdan-based fluorescent probes, which require precise quantification of spectral shifts to determine the Generalized Polarization (GP) index.

However, the collaborative nature of this international environment highlighted a critical bottleneck: data fragmentation. Different spectrometers exported proprietary formats (e.g., JCAMP-DX), and the diverse operating systems used by the team members (Italian, French, and American locales) caused frequent compatibility issues regarding decimal separators (comma vs. dot). Furthermore, proprietary formats like .dx are often ill-suited for rapid mathematical operations. To address these challenges, a custom suite of Python-based software tools was developed. These utilities were designed to standardize raw data into universal formats (DX2CSV/MergeCSV) and to perform advanced spectral deconvolution for accurate GP calculation (Extrapolator).

5.2 Spectral Data Standardization Suite: DX2CSV and MergeCSV

5.2.1 The need for standardization

Raw spectral data is often trapped in instrument-specific formats like JCAMP-DX (.dx), which are not natively supported by standard analysis software (e.g., Excel, Origin, Python Pandas). While these files contain rich metadata, they hinder quick arithmetic operations. Converting data into

Comma-Separated Values (CSV) is essential for facilitating downstream calculations—such as determining ratios for GP analysis—and ensuring that data is accessible regardless of the proprietary software used for acquisition.

5.2.2 Functionality and locale management

Two companion utilities were developed to streamline this conversion process:

- **DX2CSV**: Specifically designed to parse batch directories of .dx files, extracting the XY spectral data and metadata headers (Figure 23a).
- **MergeCSV**: Designed to combine multiple individual CSV files into a single, unified dataset matrix (Figure 23b).

A critical feature of this suite is its locale-aware parsing engine. In a mixed international environment, a file generated on a French PC (using a comma for decimals: 0,123) often causes parsing errors when opened on US/International systems (which expect a dot: 0.123). Both tools include an auto-detection algorithm and manual override options to normalize these separators during export, ensuring total interoperability among the research group members.

Master axis alignment

To merge heterogeneous spectra into a single matrix, the software constructs a global "Master X-Axis" (Wavelength). Crucially, the alignment algorithm avoids interpolation: it maps input spectra onto the unified axis only where exact wavelength matches occur, populating missing points with NaN. This conservative approach preserves the scientific integrity of the raw experimental data.

Pseudocode

```
BEGIN Spectra_Unifier (Input: DX or CSV)

    // --- 1. Initialization & Locale Setup ---
```

```
    DETECT System_Locale (EU vs US)
    SELECT     Output_Format     (e.g.,     Decimal=".",
Separator=";")

    // --- 2. Batch Parsing ---
    FOR EACH File IN Directory:
        IF Input_Type IS "DX":
            Raw_Data  =  PARSE_JCAMP(File)  //  Extract
##XYDATA
        ELSE:
            Raw_Data = PARSE_CSV(File)

        ADD Raw_Data.X_Values TO Master_X_Axis
        STORE Raw_Data IN Spectra_Collection

    // --- 3. Data Alignment (No Interpolation) ---
    SORT Master_X_Axis Ascending
    INITIALIZE Unified_Matrix

    FOR EACH Spectrum IN Spectra_Collection:
        ALIGN Spectrum.Y_Values TO Master_X_Axis (Match
Exact X only)
        ADD TO Unified_Matrix

    // --- 4. Export ---
    EXPORT        "unified_spectra_data.csv"        WITH
Selected_Format

END
```

Both codes are available on GitHub under MIT license at:

https://github.com/DavideRmni/DX2CSV

https://github.com/DavideRmni/mergecsv

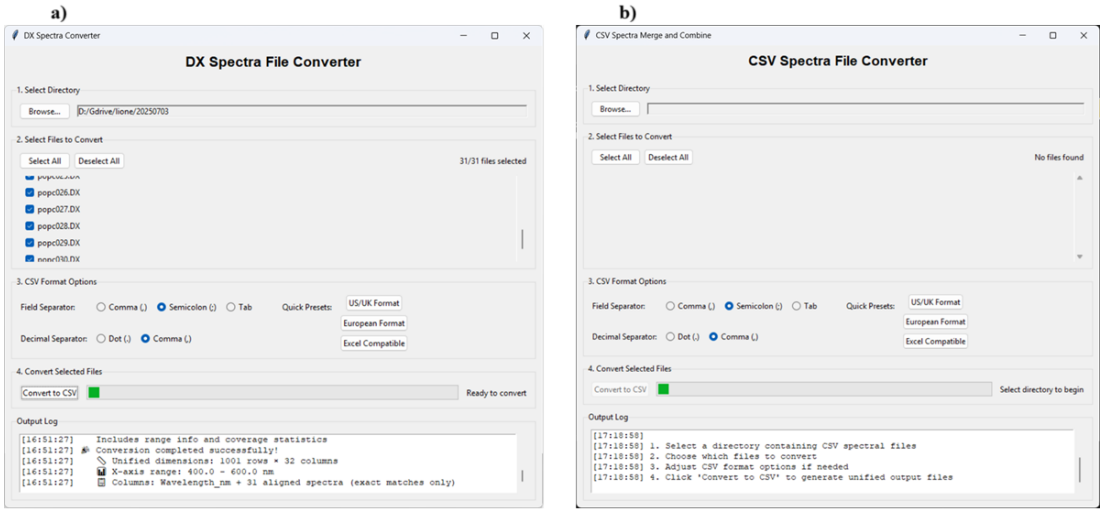

Figure 23 *Graphical User Interfaces of the standardization suite. (A) DX2CSV converting proprietary spectra. (B) MergeCSV combining datasets. Both tools allow the user to enforce specific decimal/field separators for cross-platform compatibility.*

5.3 Advanced Spectral Analysis: The Extrapolator tool

5.3.1 Scientific rationale: Generalized Polarization (GP)

The primary application of the Laurdan-based probes used in this study, such as those developed to overcome the limitations of standard Laurdan [147], is the determination of the Generalized Polarization (GP). This metric, originally introduced by Parasassi et al. [148], quantifies the hydration and order (flexibility) of the lipid bilayer by analyzing the spectral shift of the emission. The GP is calculated from the fluorescence intensities at two specific wavelengths, typically representing the gel phase ($\lambda_{blue}\approx440$) and the liquid-crystalline phase (($\lambda_{red}\approx490$) used in Equation 8.

Relying on simple intensity readings at fixed wavelengths can be inaccurate due to spectral noise, peak shifts, or overlapping contributions. To overcome this, the Extrapolator tool was developed to perform spectral deconvolution, isolating the true contributions of the two emission bands.

5.3.2 Deconvolution and analysis workflow

Extrapolator integrates preprocessing and fitting into a single Python GUI:

- **Data Import and Preprocessing** (Figure 24a): The interface allows for the batch loading of CSV files. A critical preprocessing step is the blank correction: the software calculates the average background signal from selected "blank" samples and subtracts it from the active dataset. Panel (a) shows the visualization of raw spectra (colored lines) alongside the computed average blank (dashed black line).
- **Parameter Configuration** (Figure 24b, 24c): The analysis tab provides granular control over the fitting engine. Users can select the mathematical model (Gaussian, Lorentzian, or Voigt) and the optimization algorithm (e.g., differential_evolution). To ensure biophysical relevance, peak centers can be fixed or constrained (e.g., around 440 nm and 490 nm).
- **Spectral Deconvolution** (Figure 24d): The core algorithm decomposes the complex fluorescence spectrum into individual sub-components. As illustrated in the plots, the raw signal (black line) is perfectly fitted (red line, $R^2 > 0.99$) by the sum of two distinct Voigt components (dashed blue lines).
- **Quantitative Output**: The software generates a detailed report containing the calculated area, amplitude, and FWHM for each peak. These area values are then automatically used to compute the GP index, providing a robust metric derived from the entire spectral band rather than single data points.

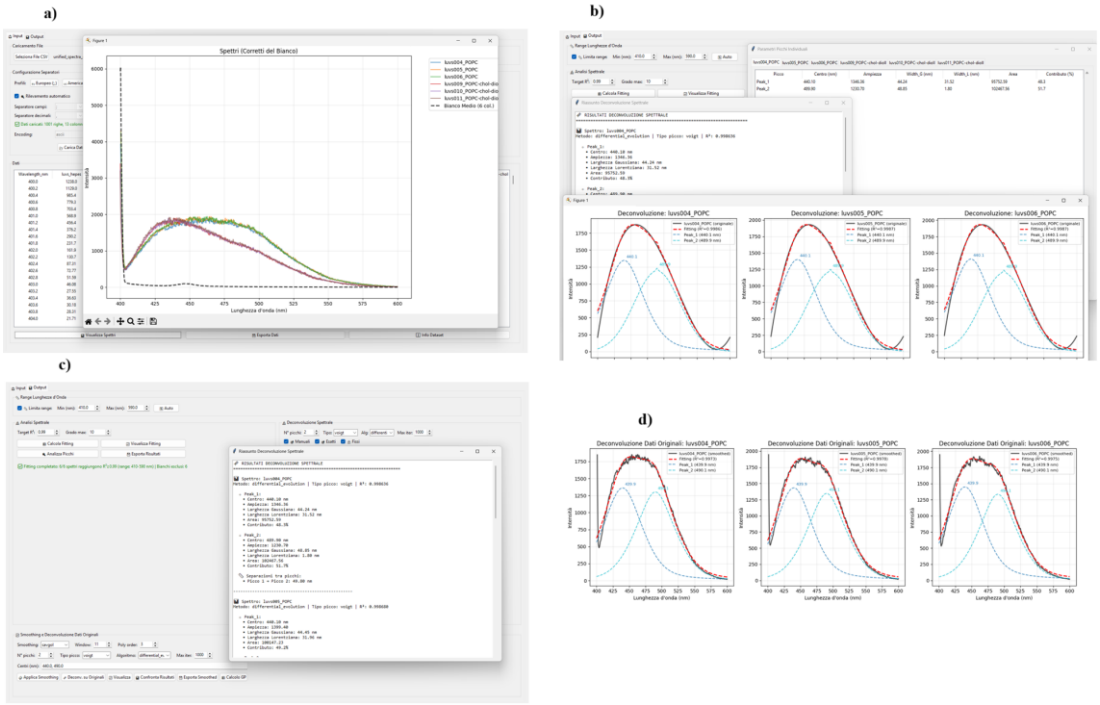

Figure 24 *The Extrapolator interface workflow. (a) Input tab showing raw fluorescence spectra and the calculated average blank (dashed black line) for background subtraction. (b) Detailed results window displaying peak parameters (Area, Amplitude) and the graphical deconvolution of multiple samples.* ***(c)*** *Analysis control panel, allowing the selection of peak models (Voigt), algorithms, and manual constraints.* ***(d)*** *Graphical output showing the deconvolution of the emission spectrum into two distinct sub-components centered at ≈440nm and ≈490nm*

Pseudocode

```
BEGIN Deconvolution_Routine

    INPUT Raw_Spectrum (X, Y)
    INPUT Targets (Center1=440, Center2=490)

    // --- 1. Preprocessing ---
    Y_Corr = Y - Blank_Spectrum
    Y_Smooth = SAVGOL_FILTER(Y_Corr)

    // --- 2. Model Definition (Voigt) ---
    DEFINE Composite_Model(x, params):
        Sum = 0
        FOR i FROM 1 TO N_Peaks:
            Sum += Amplitude[i] * Voigt(x, Center[i],
Sigma[i], Gamma[i])
        RETURN Sum

    // --- 3. Global Optimization ---
    // Constrain centers around 440nm and 490nm
```

```
    SET Bounds FOR Center[1] = [435, 445]
    SET Bounds FOR Center[2] = [485, 495]

    Result = DIFFERENTIAL_EVOLUTION(
        Objective        =        Sum((Y_Smooth        -
Composite_Model(X))²)
    )

    // --- 4. GP Extraction ---
    Area_440 = INTEGRATE(Peak_1)
    Area_490 = INTEGRATE(Peak_2)

    GP_Value  =  (Area_440  -  Area_490)  /  (Area_440  +
Area_490)

    EXPORT GP_Value, R_Squared, Fitted_Curves

END
```

The source code implementing this algorithm is released under the MIT License, and available at:

https://github.com/DavideRmni/Gp_calculator

5.3.3 Validation and enhanced sensitivity

To validate the efficacy of the Extrapolator suite, a comparative analysis was performed on two distinct lipid systems: pure **POPC** (fluid phase) and a **POPC:Cholesterol** mixture (rigid/ordered phase). The Generalized Polarization (GP) was calculated using three different methods extracted by the software:

- **Raw Curve Height**: Traditional ratio using intensities at fixed wavelengths from the raw spectrum.
- **Deconvoluted Peak Height:** Ratio using the amplitude of the fitted Voigt components.
- **Deconvoluted Peak Area:** Ratio using the integrated area of the Voigt components.

As presented in Table 5, the deconvolution-based approach demonstrates superior sensitivity.

- Dynamic Range: The standard method (GP_*Height-curve*) shows a shift (ΔG) of approximately 0.20 between the fluid POPC samples (≈0.02) and the rigid Cholesterol mixtures (≈0.22). In contrast, the Deconvoluted Area method (GP_Aree_Deconv) amplifies this distinction, showing a shift of approximately 0.51 (from ≈0.02 to ≈0.49).
- Discrimination: By resolving the overlapping spectral bands, the deconvolution algorithm effectively filters out noise and band broadening, providing a more robust metric for assessing membrane fluidity changes induced by cholesterol.

Sample	GP Height curve	GP Aree Deconv	GP height peaks deconvoluted	GP Aree Original	GP Height peaks original
luvs004_POPC	0,01249	-0,03388	0,044882	-0,02738	0,022521
luvs005_POPC	0,031211	-0,01675	0,056713	-0,01992	0,031579
luvs006_POPC	0,033082	-0,00682	0,063794	0,000722	0,040912
luvs009_POPC-chol	0,22308	0,482583	0,515507	0,4341	0,496181
luvs010_POPC-chol	0,223907	0,490997	0,523619	0,438967	0,502707
luvs011_POPC-chol	0,225959	0,495988	0,531023	0,500029	0,548775

Table 5 *Comparison of GP values calculated via different algorithms. The deconvolution methods (Area/Height) provide a sharper distinction between fluid (POPC) and rigid (POPC-Chol) membranes compared to raw curve readings.*

This validation confirms that the Extrapolator tool not only automates the analysis but significantly enhances the analytical resolution of fluorescence data in membrane biophysics.

CHAPTER 6

Conclusions and Future Prospectives

6.1 Summary of Findings

This doctoral thesis focused on the development of accessible, automated, and modular tools for membrane biophysics, addressing the technological and economic barriers that often limit research in drug discovery and development. By integrating open-source hardware, rapid prototyping, and custom software, three interconnected platforms were successfully engineered and validated, establishing a complete workflow from model membrane production to data analysis.

6.1.1 The automated Langmuir-Blodgett trough

The first major contribution is the realization of a fully functional, Arduino-based Langmuir-Blodgett trough.

- **Accessibility and Cost**: The system was engineered to be cost-effective, offering a modular alternative to commercial systems that could be too expensive.
- **Performance:** Validation tests using anionic surfactants (SLES) demonstrated a Signal-to-Noise Ratio (SNR) of 42.1 dB, confirming high sensitivity. Despite mechanical challenges of a project like this, the system successfully acquired pressure-area isotherms of complex biological samples.
- **Control Software**: The development of the LanGUImuir interface and the ScriptMaker utility bridged the gap between prototype hardware and laboratory standards, enabling automated scripting and real-time data visualization.

6.1.2 Optimized GUVs electroformation

The second contribution involved the optimization of Giant Unilamellar Vesicle (GUV) production using novel electrode geometries.

- **Material Innovation**: We validated stainless steel mesh (304/316L) as a superior alternative to traditional Indium Tin Oxide (ITO) electrodes, offering excellent chemical stability and mechanical durability.
- **Efficiency and precision**: Through the systematic evaluation of four chamber designs, Chamber D (Mesh 30) was identified as the optimal configuration. Under optimized electrical parameters (4.4 Vpp, 500 Hz), it achieved a lipid incorporation yield of 0.20%.
- **Versatility and thermal control**: The platform proved robust for investigating membrane rigidity (GP) in complex mixtures (POPC:Chol). Importantly, the system demonstrated the capability to operate at elevated temperatures (>55°C), successfully generating vesicles from high-transition temperature lipids (e.g., DPPC:DPPS:DLPC). The observed structural collapse of these specific vesicles upon cooling to room temperature confirms the system's ability to faithfully reproduce thermodynamic phase behaviors, highlighting the importance of maintaining the lipid bilayer above its phase transition temperature (Tm) during handling. Additionally, the operational flexibility allowed for the intentional generation of Multi-Lamellar Vesicles (MLVs) to facilitate translocation assays (CPP).

6.1.3 Comprehensive computational framework

Recognizing that hardware is only half of the solution, a suite of custom software tools was developed to streamline data processing and analysis in a multi-instrumental environment.

- **Standardization:** The DX2CSV and MergeCSV utilities solved critical interoperability issues, standardizing spectral data from diverse instruments and locales into a unified format.
- **Advanced Analysis:** The Extrapolator suite introduced a sophisticated pipeline for spectral deconvolution. By resolving complex fluorescence spectra into Voigt components, it enabled the precise calculation of Generalized Polarization (GP) based on peak areas. Validation tests confirmed that this method offers a significantly higher dynamic range and sensitivity compared to traditional height-based ratios.

6.1.4 Implications in drug discovery

The integration of these platforms creates a comprehensive ecosystem for lipid research. The Langmuir trough allows for the precise characterization of drug-membrane interactions at the monolayer level, providing thermodynamic data on insertion and permeability. Complementarily, the optimized electroformation setup enables the rapid production of biomimetic vesicles (GUVs/MLVs) for studying these interactions in a bilayer context. Finally, the software toolkit ensures that the data generated is processed rapidly and accurately.

Crucially, the ability to finely characterize membrane physical properties—specifically **fluidity and rigidity** via the GP index—opens new avenues for the design of **"smart bullets"** in oncology. As hypothesized by **Maniti and colleagues**, optimizing the viscoelastic properties of the lipid bilayer allows for the engineering of fusogenic carriers that selectively target cancer cells based on differential membrane dynamics rather than traditional ligand-receptor interactions. This physical targeting strategy, validated by the precise metrics provided by our *Extrapolator* suite, facilitates a multi-scale, high-throughput approach to screening pharmaceutical compounds, reducing reliance on expensive proprietary equipment.

6.1.5 Limitations and future directions

While the primary objectives of this work were met, several avenues for improvement remain:

- **Mechanical Refinement**: The Langmuir trough would benefit from precision-machined guide rails and active vibration isolation to further reduce the noise floor.
- **Sample Handling**: To fully exploit the system's capability to form high-T_g vesicles, future setups should integrate a temperature-controlled microscopy stage to prevent phase transition-induced rupture during observation.
- **Functional Expansion**: The modular architecture allows for the integration of external devices via the Arduino serial ports. Future developments will focus on interfacing additional sensors (e.g., optical probes) or actuators (e.g., the demonstrated UV-LED module) to create multi-parametric experimental setups controlled by a single central unit.
- **Automation**: Future iterations of the GUV setup could integrate automated liquid handling for lipid deposition and vesicle harvesting, further reducing operator variability.

In conclusion, this thesis demonstrates that high-quality biophysical data can be obtained using open-source, custom-built instrumentation. The developed platforms not only reduce the barrier to entry for advanced membrane research but also offer a degree of modularity and customization that proprietary systems cannot match, paving the way for more flexible and innovative experimental protocols in pharmaceutical sciences.

References

1. Boban, Z., et al., *Giant Unilamellar Vesicle Electroformation: What to Use, What to Avoid, and How to Quantify the Results.* Membranes, 2021. **11**(11): p. 860.

2. Knobloch, J., et al., *Membrane-drug interactions studied using model membrane systems.* Saudi J Biol Sci, 2015. **22**(6): p. 714-8.

3. Peetla, C., A. Stine, and V. Labhasetwar, *Biophysical interactions with model lipid membranes: applications in drug discovery and drug delivery.* Mol Pharm, 2009. **6**(5): p. 1264-76.

4. Fernandes, E., et al., *Lipid Microfluidic Biomimetic Models for Drug Screening: A Comprehensive Review.* Advanced Functional Materials, 2024. **34**(24): p. 2315166.

5. Rehman, M., et al., *Lipid-Based Nanoformulations for Drug Delivery: An Ongoing Perspective.* Pharmaceutics, 2024. **16**(11).

6. Chen, C., et al., *Characterization of lipid-based nanomedicines at the single-particle level.* Fundam Res, 2023. **3**(4): p. 488-504.

7. Bompard, J., et al., *Membrane fluidity as a new means to selectively target cancer cells with fusogenic lipid carriers.* Langmuir, 2020. **36**(19): p. 5134-5144.

8. Faizi, H.A., et al., *Fluctuation spectroscopy of giant unilamellar vesicles using confocal and phase contrast microscopy.* Soft Matter, 2020. **16**(39): p. 8996-9001.

9. Allen, T.M. and P.R. Cullis, *Liposomal drug delivery systems: from concept to clinical applications.* Advanced drug delivery reviews, 2013. **65**(1): p. 36-48.

10. Bozzuto, G. and A. Molinari, *Liposomes as nanomedical devices.* International journal of nanomedicine, 2015: p. 975-999.

11. Maget-Dana, R., *The monolayer technique: a potent tool for studying the interfacial properties of antimicrobial and membrane-lytic peptides and their interactions with lipid membranes.* Biochimica et Biophysica Acta (BBA)-Biomembranes, 1999. **1462**(1-2): p. 109-140.

12. Zhao, W., et al., *Atomic-scale structure and electrostatics of anionic palmitoyloleoylphosphatidylglycerol lipid bilayers with Na+ counterions.* Biophysical journal, 2007. **92**(4): p. 1114-1124.

13. Veatch, S.L. and S.L. Keller, *Separation of liquid phases in giant vesicles of ternary mixtures of phospholipids and cholesterol.* Biophysical journal, 2003. **85**(5): p. 3074-3083.

14. Simons, K. and J.L. Sampaio, *Membrane organization and lipid rafts*. Cold Spring Harbor perspectives in biology, 2011. **3**(10): p. a004697.

15. Rich, R.L. and D.G. Myszka, *Survey of the year 2007 commercial optical biosensor literature*. Journal of Molecular Recognition: An Interdisciplinary Journal, 2008. **21**(6): p. 355-400.

16. Lakowicz, J.R., *Principles of fluorescence spectroscopy*. 2006: Springer.

17. Möhwald, H., *Phospholipid monolayers*, in *Handbook of biological physics*. 1995, Elsevier. p. 161-211.

18. Ezsias, B., et al., *Protein reconstitution into giant unilamellar vesicles from native nanodiscs*. Biophysical Journal, 2023. **122**(3): p. 448a.

19. Yan, N., *A glimpse of membrane transport through structures—advances in the structural biology of the GLUT glucose transporters*. Journal of molecular biology, 2017. **429**(17): p. 2710-2725.

20. Marrink, S.J., et al., *Computational modeling of realistic cell membranes*. Chemical reviews, 2019. **119**(9): p. 6184-6226.

21. Denisov, I.G. and S.G. Sligar, *Nanodiscs in membrane biochemistry and biophysics*. Chemical reviews, 2017. **117**(6): p. 4669-4713.

22. Seddon, A.M., P. Curnow, and P.J. Booth, *Membrane proteins, lipids and detergents: not just a soap opera*. Biochimica et Biophysica Acta (BBA)-Biomembranes, 2004. **1666**(1-2): p. 105-117.

23. Morrell, N.T., et al., *Liposomal packaging generates Wnt protein with in vivo biological activity*. PLoS One, 2008. **3**(8): p. e2930.

24. Zhan, T., N. Rindtorff, and M. Boutros, *Wnt signaling in cancer*. Oncogene, 2017. **36**(11): p. 1461-1473.

25. Sun, C., et al., *Membrane Vesicles as Drug Delivery Systems: Source, Preparation, Modification, Drug Loading, In Vivo Administration and Biodistribution, and Application in Various Diseases*. Pharmaceutics, 2023. **15**(7).

26. Lohner, K., *New strategies for novel antibiotics: peptides targeting bacterial cell membranes*. General physiology and biophysics, 2009. **28**(2): p. 105-116.

27. Gomes-da-Silva, L.C., et al., *Lipid-based nanoparticles for siRNA delivery in cancer therapy: paradigms and challenges*. Accounts of chemical research, 2012. **45**(7): p. 1163-1171.

28. Cullis, P.R. and M.J. Hope, *Lipid nanoparticle systems for enabling gene therapies*. Molecular Therapy, 2017. **25**(7): p. 1467-1475.

29. Danaei, M., et al., *Impact of particle size and polydispersity index on the clinical applications of lipidic nanocarrier systems.* Pharmaceutics, 2018. **10**(2): p. 57.

30. Patil, Y.P. and S. Jadhav, *Novel methods for liposome preparation*. Chemistry and physics of lipids, 2014. **177**: p. 8-18.

31. Discher, D.E. and A. Eisenberg, *Polymer vesicles.* Science, 2002. **297**(5583): p. 967-973.

32. Pattni, B.S., V.V. Chupin, and V.P. Torchilin, *New developments in liposomal drug delivery.* Chemical reviews, 2015. **115**(19): p. 10938-10966.

33. Rosenblum, D., et al., *Progress and challenges towards targeted delivery of cancer therapeutics.* Nature communications, 2018. **9**(1): p. 1410.

34. Fernandes, E., C.M. Lopes, and M. Lúcio, *Lipid Biomimetic Models as Simple Yet Complex Tools to Predict Skin Permeation and Drug-Membrane Biophysical Interactions*. Pharmaceutics, 2024. **16**(6).

35. Ndeye Rokhaya, F., et al., *Phase Behavior and Structure Properties of Supported Lipid Monolayers and Bilayers in Interaction with Silica Nanoparticles*. 2013.

36. Reimhult, E. and K. Kumar, *Membrane biosensor platforms using nano- and microporous supports.* Trends Biotechnol, 2008. **26**(2): p. 82-9.

37. Banerjee, S. and Y.L. Lyubchenko, *Topographically smooth and stable supported lipid bilayer for high-resolution AFM studies.* Methods, 2022. **197**: p. 13-19.

38. Richter, R.P., R. Bérat, and A.R. Brisson, *Formation of solid-supported lipid bilayers: an integrated view.* Langmuir, 2006. **22**(8): p. 3497-3505.

39. Seddon, A.M., P. Curnow, and P.J. Booth, *Membrane proteins, lipids and detergents: not just a soap opera*. Biochim Biophys Acta, 2004. **1666**(1-2): p. 105-17.

40. Aytar Çelik, P., et al., *Bacterial Membrane Vesicles as Smart Drug Delivery and Carrier Systems: A New Nanosystems Tool for Current Anticancer and Antimicrobial Therapy.* Pharmaceutics, 2023. **15**(4).

41. Le, Q.V., et al., *Cell membrane-derived vesicles for delivery of therapeutic agents*. Acta Pharm Sin B, 2021. **11**(8): p. 2096-2113.

42. Srivatsav, A.T. and S. Kapoor, *The Emerging World of Membrane Vesicles: Functional Relevance, Theranostic Avenues and Tools for Investigating Membrane Function.* Front Mol Biosci, 2021. **8**: p. 640355.

43. Dimova, R. and C. Marques, *The giant vesicle book*. 2019: CRC Press.

44. Gregoriadis, G., *Liposome research in drug delivery: the early days.* Journal of Drug Targeting, 2008. **16**(7-8): p. 520-524.

45. Macher, M., et al., *An Efficient Method for the Production of High-Purity Bioinspired Large Unilamellar Vesicles*. ACS Synthetic Biology, 2024. **13**(3): p. 781-791.

46. Gregoriadis, G., *Liposome Technology: Entrapment of drugs and other materials into liposomes*. Vol. 2. 2016: CRC Press.

47. Grimaldi, N., et al., *Lipid-based nanovesicles for nanomedicine*. Chemical society reviews, 2016. **45**(23): p. 6520-6545.

48. Alves, N.J., K.B. Turner, and S.A. Walper, *Directed protein packaging within outer membrane vesicles from Escherichia coli: design, production and purification*. Journal of visualized experiments: JoVE, 2016(117): p. 54458.

49. Zheng, Y., *Synthesis, Characterization and Application of Polymer-Grafted Nanoparticles*. 2017, University of South Carolina.

50. Vipanchi, V., M. Fatima, and P. Domaraju, *Quality by Design approach for nanosystem based topical drug delivery*. German Journal of Pharmaceuticals and Biomaterials, 2023. **2**(1): p. 1-17.

51. Bhargava, L., *Transfection Of Ionizable Lipid Nanoparticles On Raw 264.7 And Mda-Mb-231*. 2024: Missouri University of Science and Technology.

52. Chakif, D., *Comparative Study of Chelating Agents in the Treatment of Heavy Metal Poisoning on Early Zebrafish Embryo Development followed by Quantitative PCR Studies*. Universität Bern.

53. Uzun, H.D., et al., *Electroformation of giant unilamellar vesicles from large liposomes*. The European Physical Journal Special Topics, 2024. **233**.

54. Okumura, Y. and T. Sugiyama, *Electroformation of giant vesicles on a polymer mesh*. Membranes, 2011. **1**(3): p. 184-194.

55. Garten, M., et al., *Reconstitution of a transmembrane protein, the voltage-gated ion channel, KvAP, into giant unilamellar vesicles for microscopy and patch clamp studies*. Journal of visualized experiments: JoVE, 2015(95): p. 52281.

56. Méléard, P., L.A. Bagatolli, and T. Pott, *Giant unilamellar vesicle electroformation: From lipid mixtures to native membranes under physiological conditions*. Methods in enzymology, 2009. **465**: p. 161-176.

57. Mombayashi, D., et al., *Factors Facilitating Fusion between Dye-encapsulating Vesicles and Giant Unilamellar Vesicles*. Sensors and Materials, 2021. **33**(12): p. 4361-4369.

58. Cheng, Y., et al., *Microfluidic technologies for lipid vesicle generation*. Lab on a Chip, 2024. **24**(20): p. 4679-4716.

59. Deshpande, S., et al., *Octanol-assisted liposome assembly on chip*. Nature Communications, 2016. **7**(1): p. 10447.

60. Maeki, M., et al., *Microfluidic technologies and devices for lipid nanoparticle-based RNA delivery*. Journal of Controlled Release, 2022. **344**: p. 80-96.

61. Prakash, G., et al., *Microfluidic fabrication of lipid nanoparticles for the delivery of nucleic acids*. Advanced drug delivery reviews, 2022. **184**: p. 114197.

62. Piunti, C. and E. Cimetta, *Microfluidic approaches for producing lipid-based nanoparticles for drug delivery applications*. Biophysics Reviews, 2023. **4**(3).

63. Carugo, D., et al., *Liposome production by microfluidics: potential and limiting factors*. Scientific reports, 2016. **6**(1): p. 25876.

64. Vorselen, D., et al., *Mechanical characterization of liposomes and extracellular vesicles, a protocol*. Frontiers in molecular biosciences, 2020. **7**: p. 139.

65. Morris, E.J., et al., *The Physical Characterization of Extracellular Vesicles for Function Elucidation and Biomedical Applications: A Review*. Particle & Particle Systems Characterization, 2024. **41**(10): p. 2400024.

66. Jass, J., T. Tjärnhage, and G. Puu, *From liposomes to supported, planar bilayer structures on hydrophilic and hydrophobic surfaces: an atomic force microscopy study*. Biophysical journal, 2000. **79**(6): p. 3153-3163.

67. Reviakine, I. and A. Brisson, *Formation of supported phospholipid bilayers from unilamellar vesicles investigated by atomic force microscopy*. Langmuir, 2000. **16**(4): p. 1806-1815.

68. Hoo, C.M., et al., *A comparison of atomic force microscopy (AFM) and dynamic light scattering (DLS) methods to characterize nanoparticle size distributions*. Journal of Nanoparticle Research, 2008. **10**(Suppl 1): p. 89-96.

69. Sezgin, E., et al., *The mystery of membrane organisation: composition, regulation and physiological relevance of lipid rafts*. Nat. Rev. Mol. Cell Biol, 2017.

70. McConnell, H.M., *Structures and transitions in lipid monolayers at the air-water interface*. Annual Review of Physical Chemistry, 1991. **42**(1): p. 171-195.

71. Bağcı, C., et al., *Overview of extracellular vesicle characterization techniques and introduction to combined reflectance and fluorescence confocal microscopy to distinguish extracellular vesicle subpopulations*. Neurophotonics, 2022. **9**(2): p. 021903-021903.

72. Meyvis, T.K., et al., *Fluorescence recovery after photobleaching: a versatile tool for mobility and interaction measurements in pharmaceutical research*. Pharmaceutical research, 1999. **16**(8): p. 1153-1162.

73. Kang, M., et al., *Simplified equation to extract diffusion coefficients from confocal FRAP data*. Traffic, 2012. **13**(12): p. 1589-1600.

74. Stavrakis, S., et al., *Measuring concentration and diffusivity within biomolecular condensates using calibration-free scanning fluorescence correlation spectroscopy.* Chemical Science, 2025.

75. Ries, J. and P. Schwille, *Fluorescence correlation spectroscopy.* BioEssays, 2012. **34**(5): p. 361-368.

76. Simões, M.G., et al., *Quantification and Imaging of Nanoscale Contact with Förster Resonance Energy Transfer.* ACS Applied Materials & Interfaces, 2021. **13**(16): p. 19521-19529.

77. Loura, L.M., et al., *FRET analysis of domain formation and properties in complex membrane systems*. Biochimica et Biophysica Acta (BBA)-Biomembranes, 2009. **1788**(1): p. 209-224.

78. Suhling, K., P.M. French, and D. Phillips, *Time-resolved fluorescence microscopy.* Photochemical & Photobiological Sciences, 2005. **4**(1): p. 13-22.

79. Volpe, C.D. and S. Siboni, *The Wilhelmy method: a critical and practical review*. Surface Innovations, 2018. **6**(3): p. 120-132.

80. Behnecke, M., et al., *Wilhelmy balance—A simple and reliable method for determining immersion angles and surface energies even on non-planar and complex geometries?* Surface and Interface Analysis, 2024. **56**(4): p. 212-220.

81. Davies, J.T., *Interfacial phenomena*. 2012: Elsevier.

82. Blodgett, K.B., *Films built by depositing successive monomolecular layers on a solid surface*. Journal of the American Chemical Society, 1935. **57**(6): p. 1007-1022.

83. Ariga, K., et al., *25th Anniversary article: What can be done with the Langmuir-Blodgett method? Recent developments and its critical role in materials science*. Advanced Materials, 2013. **25**(45): p. 6477-6512.

84. Kurniawan, J., et al., *Preparation and characterization of solid-supported lipid bilayers formed by Langmuir–Blodgett deposition: a tutorial*. Langmuir, 2018. **34**(51): p. 15622-15639.

85. Rana, D., et al., *Surface functionalization of nanobiomaterials for application in stem cell culture, tissue engineering and regenerative medicine*. Vol. 32. 2016.

86. Heimburg, T., *Thermal biophysics of membranes*. 2008: John Wiley & Sons.

87. Patching, S.G., *Surface plasmon resonance spectroscopy for characterisation of membrane protein–ligand interactions and its potential for drug discovery*. Biochimica et Biophysica Acta (BBA)-Biomembranes, 2014. **1838**(1): p. 43-55.

88. Reviakine, I., D. Johannsmann, and R.P. Richter, *Hearing what you cannot see and visualizing what you hear: interpreting quartz crystal microbalance data from solvated interfaces*. 2011, ACS Publications.

89. Filipe, V., A. Hawe, and W. Jiskoot, *Critical evaluation of Nanoparticle Tracking Analysis (NTA) by NanoSight for the measurement of nanoparticles and protein aggregates.* Pharmaceutical research, 2010. **27**(5): p. 796-810.

90. Gandham, S., et al., *Technologies and standardization in research on extracellular vesicles.* Trends in biotechnology, 2020. **38**(10): p. 1066-1098.

91. Anastas, P. and N. Eghbali, *Green chemistry: principles and practice.* Chemical society reviews, 2010. **39**(1): p. 301-312.

92. Bulbake, U., et al., *Liposomal formulations in clinical use: an updated review.* Pharmaceutics, 2017. **9**(2): p. 12.

93. Menichetti, R., K.H. Kanekal, and T. Bereau, *Drug–membrane permeability across chemical space.* ACS central science, 2019. **5**(2): p. 290-298.

94. Kulkarni, M.P., P.S.S. Kiran, and R. Kumar, *Liposomal Drug Delivery: Therapeutic Applications in Chronic Respiratory Diseases*, in *Advanced Drug Delivery Strategies for Targeting Chronic Inflammatory Lung Diseases*, D.K. Chellappan, K. Pabreja, and M. Faiyazuddin, Editors. 2022, Springer Singapore: Singapore. p. 471-492.

95. Kahya, N., *Protein–protein and protein–lipid interactions in domain-assembly: Lessons from giant unilamellar vesicles.* Biochimica et Biophysica Acta (BBA) - Biomembranes, 2010. **1798**(7): p. 1392-1398.

96. Dhanawat, G., et al., *Invagination of Giant Unilamellar Vesicles upon Membrane Mixing with Native Vesicles.* ACS Omega, 2024. **9**(46): p. 46615-46626.

97. Subhan, M.A., et al., *Recent Advances in Tumor Targeting via EPR Effect for Cancer Treatment.* Journal of Personalized Medicine, 2021. **11**(6): p. 571.

98. Behzadi, S., et al., *Cellular uptake of nanoparticles: journey inside the cell.* Chemical Society Reviews, 2017. **46**(14): p. 4218-4244.

99. Kam, N.W.S. and H. Dai, *Carbon Nanotubes as Intracellular Protein Transporters: Generality and Biological Functionality.* Journal of the American Chemical Society, 2005. **127**(16): p. 6021-6026.

100. Patra, J.K., et al., *Nano based drug delivery systems: recent developments and future prospects.* Journal of nanobiotechnology, 2018. **16**(1): p. 71.

101. Sercombe, L., et al., *Advances and Challenges of Liposome Assisted Drug Delivery.* Front Pharmacol, 2015. **6**: p. 286.

102. Pande, S., *Liposomes for drug delivery: review of vesicular composition, factors affecting drug release and drug loading in liposomes*. Artificial Cells, Nanomedicine, and Biotechnology, 2023. **51**(1): p. 428-440.

103. Lombardo, D., et al., *Soft Interaction in Liposome Nanocarriers for Therapeutic Drug Delivery*. Nanomaterials (Basel), 2016. **6**(7).

104. Lichtman, J.W. and J.-A. Conchello, *Fluorescence microscopy*. Nature methods, 2005. **2**(12): p. 910-919.

105. Reits, E.A. and J.J. Neefjes, *From fixed to FRAP: measuring protein mobility and activity in living cells*. Nature cell biology, 2001. **3**(6): p. E145.

106. Vogel, S.S., C. Thaler, and S.V. Koushik, *Fanciful fret*. Science's STKE, 2006. **2006**(331): p. re2-re2.

107. Liu, A., et al., *Research progress in membrane fusion-based hybrid exosomes for drug delivery systems*. Frontiers in Bioengineering and Biotechnology, 2022. **10**: p. 939441.

108. Glukhova, O.E., *Liposome Drug Delivery System across Endothelial Plasma Membrane: Role of Distance between Endothelial Cells and Blood Flow Rate*. Molecules, 2020. **25**(8).

109. Landreh, M., et al., *Integrating mass spectrometry with MD simulations reveals the role of lipids in Na+/H+ antiporters*. Nature Communications, 2017. **8**(1): p. 13993.

110. Gu, W., et al., *Recent Progress in the Applications of Langmuir–Blodgett Film Technology*. Nanomaterials, 2024. **14**(12): p. 1039.

111. Fleming, J., et al., *Development and evaluation of in-situ instrumentation for cylindrical Li-ion cells using fibre optic sensors*. HardwareX, 2018. **3**: p. 100-109.

112. Pearce, J.M., *Building research equipment with free, open-source hardware*. Science, 2012. **337**(6100): p. 1303-1304.

113. Grinias, J.P., et al., *An inexpensive, open-source USB Arduino data acquisition device for chemical instrumentation*. 2016, ACS Publications.

114. Wilhelmy, L., *Ueber die Abhängigkeit der Capillaritäts-Constanten des Alkohols von Substanz und Gestalt des benetzten festen Körpers*. Annalen der Physik, 1863. **195**(6): p. 177-217.

115. Adamson, A.W. and A.P. Gast, *Physical chemistry of surfaces*. Vol. 150. 1967: Interscience publishers New York.

116. Petty, M.C., *Langmuir-blodgett films*. 1996.

117. Mitsche, M.A., L. Wang, and D.M. Small, *Adsorption of egg phosphatidylcholine to an air/water and triolein/water bubble interface: use of the 2-dimensional phase rule to estimate the surface composition of a phospholipid/triolein/water surface as a function of surface pressure.* J Phys Chem B, 2010. **114**(9): p. 3276-84.

118. Lintker, K.B., et al., *A comparison of the packing behavior of egg phosphatidylcholine with cholesterol and biogenically related sterols in Langmuir monolayer films.* Chem Phys Lipids, 2009. **161**(1): p. 22-31.

119. Marsh, D., *Water adsorption isotherms of lipids.* Biophys J, 2011. **101**(11): p. 2704-12.

120. McConnell, H.M., et al., *Supported planar membranes in studies of cell-cell recognition in the immune system.* Biochim Biophys Acta, 1986. **864**(1): p. 95-106.

121. Grakoui, A., et al., *The immunological synapse: a molecular machine controlling T cell activation.* Science, 1999. **285**(5425): p. 221-7.

122. Sackmann, E., *Supported membranes: scientific and practical applications.* Science, 1996. **271**(5245): p. 43-8.

123. Cornell, B.A., et al., *A biosensor that uses ion-channel switches.* Nature, 1997. **387**(6633): p. 580-3.

124. Staufer, O., et al., *Microfluidic production and characterization of biofunctionalized giant unilamellar vesicles for targeted intracellular cargo delivery.* Biomaterials, 2020. **264**: p. 120203.

125. Yang, J., et al., *Microbe-derived extracellular vesicles as a smart drug delivery system.* Transl Clin Pharmacol, 2018. **26**(3): p. 103-110.

126. Tanford, C., *Interfacial free energy and the hydrophobic effect.* Proceedings of the National Academy of Sciences of the United States of America, 1979. **76 9**: p. 4175-6.

127. Chandler, D., *Interfaces and the driving force of hydrophobic assembly.* Nature, 2005. **437**(7059): p. 640-7.

128. Sessa, L., et al., *Hydroxylated Fatty Acids: The Role of the Sphingomyelin Synthase and the Origin of Selectivity.* Membranes, 2021. **11**(10): p. 787.

129. Piotto, S., et al., *Differential effect of 2-hydroxyoleic acid enantiomers on protein (sphingomyelin synthase) and lipid (membrane) targets.* Biochimica et Biophysica Acta (BBA) - Biomembranes, 2014. **1838**(6): p. 1628-1637.

130. Scrima, M., et al., *Structural features of the C8 antiviral peptide in a membrane-mimicking environment.* Biochim Biophys Acta, 2014. **1838**(3): p. 1010-8.

131. Casas, J., et al., *G protein-membrane interactions II: Effect of G protein-linked lipids on membrane structure and G protein-membrane interactions*. Biochimica et Biophysica Acta (BBA) - Biomembranes, 2017. **1859**(9, Part B): p. 1526-1535.

132. Angelova, M.I. and D.S. Dimitrov, *Liposome electroformation*. Faraday discussions of the Chemical Society, 1986. **81**: p. 303-311.

133. Dimitrov, D.S. and M.I. Angelova, *Lipid swelling and liposome formation on solid surfaces in external electric fields*, in *New Trends in Colloid Science*. 1987, Springer. p. 48-56.

134. Drabik, D., J. Doskocz, and M. Przybyło, *Effects of electroformation protocol parameters on quality of homogeneous GUV populations*. Chemistry and Physics of Lipids, 2018. **212**: p. 88-95.

135. Angelova, M., et al., *Preparation of giant vesicles by external AC electric fields. Kinetics and applications*. Trends in colloid and interface science VI, 1992: p. 127-131.

136. Schmid, E.M., D.L. Richmond, and D.A. Fletcher, *Reconstitution of proteins on electroformed giant unilamellar vesicles*, in *Methods in cell biology*. 2015, Elsevier. p. 319-338.

137. Herold, C., et al., *Efficient electroformation of supergiant unilamellar vesicles containing cationic lipids on ITO-coated electrodes*. Langmuir, 2012. **28**(13): p. 5518-5521.

138. Ayuyan, A.G. and F.S. Cohen, *Lipid peroxides promote large rafts: effects of excitation of probes in fluorescence microscopy and electrochemical reactions during vesicle formation*. Biophysical journal, 2006. **91**(6): p. 2172-2183.

139. Pereno, V., et al., *Electroformation of giant unilamellar vesicles on stainless steel electrodes*. ACS omega, 2017. **2**(3): p. 994-1002.

140. Le Berre, M., et al., *Electroformation of giant phospholipid vesicles on a silicon substrate: advantages of controllable surface properties*. Langmuir, 2008. **24**(6): p. 2643-2649.

141. Bellon, J.A., M.J. Pino, and N. Wilke, *Low-cost equipment for electroformation of Giant Unilamellar Vesicles*. HardwareX, 2018. **4**: p. e00037.

142. Cooper, A. and A.B. Subramaniam, *Ultrahigh yields of giant vesicles obtained through mesophase evolution and breakup*. Soft Matter, 2024. **20**(48): p. 9547-9561.

143. Pazzi, J. and A.B. Subramaniam, *Dynamics of giant vesicle assembly from thin lipid films*. Journal of Colloid and Interface Science, 2024. **661**: p. 1033-1045.

144. Pazzi, J. and A.B. Subramaniam, *Nanoscale Curvature Promotes High Yield Spontaneous Formation of Cell-Mimetic Giant Vesicles on Nanocellulose Paper*. ACS Applied Materials & Interfaces, 2020. **12**(50): p. 56549-56561.

145. Vitkova, V., et al., *Sucrose solutions alter the electric capacitance and dielectric permittivity of lipid bilayers*. Colloids and Surfaces A: Physicochemical and Engineering Aspects, 2018. **557**: p. 51-57.

146. Vlahovska, P.M., et al., *Electrohydrodynamic model of vesicle deformation in alternating electric fields*. Biophys J, 2009. **96**(12): p. 4789-803.

147. Cheniour, M., et al., *A convenient and versatile synthesis of Laurdan-like fluorescent membrane probes: characterization of their fluorescence properties*. RSC Advances, 2016. **6**(7): p. 5547-5557.

148. Parasassi, T., et al., *Quantitation of lipid phases in phospholipid vesicles by the generalized polarization of Laurdan fluorescence*. Biophys J, 1991. **60**(1): p. 179-89.